Improved WIMP-search reach of the CDMS II germanium data

R. Agnese,[21] A. J. Anderson,[5] M. Asai,[9] D. Balakishiyeva,[21] D. Barker,[23] R. Basu Thakur,[3,22] D. A. Bauer,[3] J. Billard,[5] A. Borgland,[9] M. A. Bowles,[13] D. Brandt,[9] P. L. Brink,[9] R. Bunker,[10] B. Cabrera,[12] D. O. Caldwell,[18] R. Calkins,[11] D. G. Cerdeño,[2] H. Chagani,[23] Y. Chen,[13] J. Cooley,[11] B. Cornell,[1] C. H. Crewdson,[7] P. Cushman,[23] M. Daal,[17] P. C. F. Di Stefano,[7] T. Doughty,[17] L. Esteban,[15] S. Fallows,[23] E. Figueroa-Feliciano,[5] G. L. Godfrey,[9] S. R. Golwala,[1] J. Hall,[6] H. R. Harris,[14] S. A. Hertel,[5] T. Hofer,[23] D. Holmgren,[3] L. Hsu,[3] M. E. Huber,[19] D. Jardin,[11] A. Jastram,[14] O. Kamaev,[7] B. Kara,[11] M. H. Kelsey,[9] A. Kennedy,[23] M. Kiveni,[13] K. Koch,[23] A. Leder,[5] B. Loer,[3] E. Lopez Asamar,[15] P. Lukens,[3] R. Mahapatra,[14] V. Mandic,[23] K. A. McCarthy,[5] N. Mirabolfathi,[14] R. A. Moffatt,[12] S. M. Oser,[16] K. Page,[7] W. A. Page,[16] R. Partridge,[9] M. Pepin,[23] A. Phipps,[17] K. Prasad,[14] M. Pyle,[17] H. Qiu,[11] W. Rau,[7] P. Redl,[12] A. Reisetter,[20] Y. Ricci,[7] H. E. Rogers,[23] T. Saab,[21] B. Sadoulet,[17,4] J. Sander,[24] K. Schneck,[9] R. W. Schnee,[10] S. Scorza,[11] B. Serfass,[17] B. Shank,[12] D. Speller,[17] D. Toback,[14] S. Upadhyayula,[14] A. N. Villano,[23,*] B. Welliver,[21] J. S. Wilson,[14] D. H. Wright,[9] X. Yang,[24] S. Yellin,[12] J. J. Yen,[12] B. A. Young,[8] and J. Zhang[23]

(SuperCDMS Collaboration)

[1]*Division of Physics, Mathematics, and Astronomy, California Institute of Technology, Pasadena, California 91125, USA*
[2]*Institute for Particle Physics Phenomenology, Department of Physics, Durham University, Durham, United Kingdom*
[3]*Fermi National Accelerator Laboratory, Batavia, Illinois 60510, USA*
[4]*Lawrence Berkeley National Laboratory, Berkeley, California 94720, USA*
[5]*Department of Physics, Massachusetts Institute of Technology, Cambridge, Massachusetts 02139, USA*
[6]*Pacific Northwest National Laboratory, Richland, Washington 99352, USA*
[7]*Department of Physics, Queen's University, Kingston, Ontario K7L 3N6, Canada*
[8]*Department of Physics, Santa Clara University, Santa Clara, California 95053, USA*
[9]*SLAC National Accelerator Laboratory/Kavli Institute for Particle Astrophysics and Cosmology, Menlo Park, California 94025, USA*
[10]*Department of Physics, South Dakota School of Mines and Technology, Rapid City, South Dakota 57701, USA*
[11]*Department of Physics, Southern Methodist University, Dallas, Texas 75275, USA*
[12]*Department of Physics, Stanford University, Stanford, California 94305, USA*
[13]*Department of Physics, Syracuse University, Syracuse, New York 13244, USA*
[14]*Department of Physics and Astronomy, and the Mitchell Institute for Fundamental Physics and Astronomy, Texas A&M University, College Station, Texas 77843, USA*
[15]*Departamento de Física Teórica and Instituto de Física Teórica UAM/CSIC, Universidad Autónoma de Madrid, 28049 Madrid, Spain*
[16]*Department of Physics & Astronomy, University of British Columbia, Vancouver, British Columbia V6T 1Z1, Canada*
[17]*Department of Physics, University of California, Berkeley, California 94720, USA*
[18]*Department of Physics, University of California, Santa Barbara, California 93106, USA*
[19]*Department of Physics, University of Colorado Denver, Denver, Colorado 80217, USA*
[20]*Department of Physics, University of Evansville, Evansville, Indiana 47722, USA*
[21]*Department of Physics, University of Florida, Gainesville, Florida 32611, USA*
[22]*Department of Physics, University of Illinois at Urbana-Champaign, Urbana, Illinois 61801, USA*
[23]*School of Physics and Astronomy, University of Minnesota, Minneapolis, Minnesota 55455, USA*
[24]*Department of Physics, University of South Dakota, Vermillion, South Dakota 57069, USA*

(Received 23 April 2015; published 12 October 2015)

CDMS II data from the five-tower runs at the Soudan Underground Laboratory were reprocessed with an improved charge-pulse fitting algorithm. Two new analysis techniques to reject surface-event backgrounds were applied to the 612 kg days germanium-detector weakly interacting massive particle (WIMP)-search exposure. An extended analysis was also completed by decreasing the 10 keV analysis threshold to ~5 keV, to increase sensitivity near a WIMP mass of 8 GeV/c^2. After unblinding, there were zero candidate events above a deposited energy of 10 keV and six events in the lower-threshold analysis.

*Corresponding author.
villaa@physics.umn.edu

This yielded minimum WIMP-nucleon spin-independent scattering cross-section limits of 1.8×10^{-44} and 1.18×10^{-41} at 90% confidence for 60 and 8.6 GeV/c^2 WIMPs, respectively. This improves the previous CDMS II result by a factor of 2.4 (2.7) for 60 (8.6) GeV/c^2 WIMPs.

DOI: 10.1103/PhysRevD.92.072003 PACS numbers: 95.35.+d, 95.30.Cq, 85.25.Oj, 29.40.Wk

I. INTRODUCTION

The mass balance of the Universe is the subject of intense research and debate. Discrepancies between gravitationally determined galaxy-cluster masses and their observed luminosities provided the earliest motivation for dark matter [1,2]. Modern galactic rotation curves sharpen the argument [3–5], as do more recent studies of galaxy cluster dynamics [6,7]. Likewise, spectroscopy of intergalactic x-ray-emitting gas [6,7] and gravitational lensing [8–12] elevate these presumed mass discrepancies to the level of a crisis.

To bring the data sets into consistency requires either modifications of gravity [13,14] and/or large quantities of nonluminous matter. Observations of colliding clusters [15,16] provide evidence for excess nonluminous matter, though alternate models of gravity and some nonluminous matter can apparently also reproduce such results [17,18]. Nonrelativistic (cold) relic particle dark matter alone could resolve these discrepancies and is also considered an essential ingredient in gravitational simulations of the large-scale structure of the Universe. For example, the Via Lactea and Millennium simulations show excellent agreement with the observed large-scale structure of our Universe when cold dark matter is included [19–21].

While the observed galactic dynamics and large-scale structure naturally lead us to consider cold particle dark matter, cosmological measurements have been important in constructing a consistent model for the evolution of the Universe using such cold dark matter (CDM). The accelerating expansion of the Universe [22–24], big bang nucleosynthesis [25], baryon acoustic oscillations [26], and the cosmic microwave background [27,28] support a cosmology whose dominant components are dark energy (which could correspond to a cosmological constant Λ) and nonbaryonic CDM. When interpreted within the framework of the ΛCDM model, these cosmological measurements enable precise determination of the CDM and dark-energy content of the Universe [29].

Particle physics provides clues as to the possible identity of nonbaryonic CDM. It was realized early on that weakly interacting massive particles (WIMPs) with GeV- to TeV-scale masses could thermally freeze out in the early Universe to give the correct relic density [30]. Supersymmetry provides a WIMP candidate in the lightest supersymmetric particle and has many other benefits, like solving the hierarchy problem [31]. Still other particle physics models considered more recently [32] provide motivation for light WIMPs and linkages to the matter/antimatter asymmetry of the Universe.

WIMPs can be searched for directly through their scattering off nuclei in a terrestrial detector. Since these interactions are expected to be rare it is important for a dark-matter detector to have a low threshold (10 keV or below) and excellent background rejection capabilities. The Cryogenic Dark Matter Search (CDMS) collaboration has developed cryogenic semiconductor detectors focusing on those properties for the purpose of measuring WIMP-scattering events.

This paper explores new analysis techniques using data taken by the CDMS experiment for the direct detection of WIMPs during the CDMS II running period [33–35]. There are four data periods associated with the data set used in this work, varying from 1 to 6 months in duration. The experiment used Ge and Si detectors and was located in the Soudan Underground Laboratory at a shielding depth of 2090 m water equivalent (m.w.e.). The largest payload consisted of a total of 19 Ge (∼240 g each) and 11 Si (∼110 g each) detectors. All detectors are cylindrical, 7.6 cm in diameter, ∼1 cm in height, and arranged in five vertical stacks ("towers") each including six detectors [36,37] (see Fig. 1). The detectors are labeled TxZy where x (1–5) is the tower number and y (1–6) indicates the position within the stack (from top to bottom).

In each detector, particle interactions produce electron-hole pairs (ionization) together with phonons. The charge carriers are drifted by a small electric field (3 V/cm for Ge and 4 V/cm for Si) and collected on concentric aluminum electrodes deposited on one of the flat faces of the crystal. On the opposite face, superconducting transition-edge sensors (TESs) arranged in quadrants collect phonons before thermalization. Charge and phonons are measured independently for the purpose of event-by-event discrimination: WIMP signal events will produce a nuclear recoil (NR) in the detector, whereas most background processes produce an electron recoil (ER). The ratio of ionization to phonon signal amplitudes allows discrimination of NRs from the far greater number of ERs with a rejection factor $>10^4$ [33] in the 10–100 keV region. Lead shielding further reduced gamma-induced backgrounds, and neutron-induced NR backgrounds were reduced with polyethylene shielding. The shielding is surrounded by an active scintillator veto to tag events induced by cosmic-ray muon showers.

Recoils within ∼10 μm of the detector surface can have reduced ionization signals because of poor charge collection, which can be sufficient to misclassify a surface ER as an NR. These reduced-charge ERs originate from three major sources: electrons produced by β emitters on or

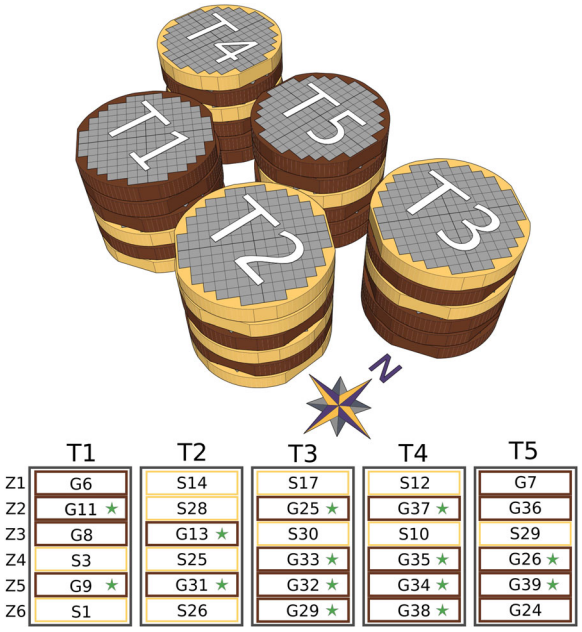

FIG. 1 (color online). Isometric representation of the CDMS II detector arrangement and tower occupation, with direction of north indicated. The ZIP detectors in each tower are numbered 1–6 and are either silicon (yellow) or germanium (brown). The identification numbers of each detector were given to track the raw material the detectors were produced from and the processing to which they were subjected. For example the detector "G9" is a germanium detector with identification number 9. Green stars indicate detectors that were used in this data analysis (see Sec. II).

near the detector surfaces, electrons ejected from photons scattering in nearby material, and photons that interact near the detector surfaces. All of these mechanisms can lead to events in which an energy deposition is observed in only a single detector, producing "surface events" that can be mistaken for single-interaction NRs. The long-lived ^{222}Rn daughter ^{210}Pb, implanted in the detector surfaces and their copper housings, is the primary source of such surface events. This class of events constitutes the dominant background for the CDMS II WIMP search and presents a considerable challenge [37]. Fortunately, recoils near detector surfaces are characterized by prompt phonon absorption in the TESs. Consequently, the phonon signals for surface ERs are (on average) faster than for NRs in the detector's bulk, enabling surface-event background discrimination based on phonon-pulse timing. The event selection criteria derived from phonon timing (called "timing cuts") presented here are essential to obtaining optimal WIMP sensitivity for the CDMS II data set because they mitigate the surface-event background, improving the overall ER rejection to $>10^6$.

Nonsignal NR events have two known sources: Ge recoils induced by scattering neutrons and ^{206}Pb nuclei from the decay of ^{210}Po near the detector surfaces. The expected neutron background for CDMS II is roughly equal parts cosmic-ray muon-induced neutrons and radiogenic neutrons from trace contaminants in the shielding and detector. Radiogenic neutrons produced outside the shielding have too little energy to cause a detectable NR after penetrating the polyethylene. By combining simulations with *in situ* data, we estimate the neutron background to be subdominant compared to the surface-event background (see Secs. VII B and VII C). The ^{206}Pb background contribution is also subdominant in this analysis.

The data set used in this work comes from the Ge detectors in the final CDMS II five-tower exposure and was acquired between July 2007 and September 2008. The total raw exposure for this running period was approximately 612 kg days. The original analysis of this data set provided world-leading sensitivity to spin-independent elastic WIMP-nucleon scattering in 2010 when it was first published [33]. Here, we reevaluate this data set using improved data reduction algorithms and surface-event rejection methods that reduce the expected surface-event contamination ("leakage") in the WIMP signal region compared with the original analysis. In the 2010 analysis a 10 keV [38] analysis threshold was used to limit the expected background to less than one event for the entire exposure. Intriguing results at low WIMP mass [39–43] motivated us additionally to examine the data with reduced thresholds.

II. CDMS II DETECTOR PROPERTIES

The CDMS II Z-sensitive ionization and phonon detectors (ZIPs) are operated at a temperature of ∼50 mK and feature six readout channels: two charge electrodes on one side and four phonon sensors on the opposite side [44]. The analysis undertaken here includes only Ge detectors, for which the ionization channels are biased with a 3 V potential across the crystal. Furthermore, five of the 19 Ge detectors were omitted from the analysis because of readout channel failures across all data sets. This gives a direct analogy to the original analysis of this data set, which used the same detector subset. Ionization channels are read out by a low-noise junction field-effect transistor circuit with an operating temperature of ∼150 K [45]. Phonons are detected by quasiparticle-trap-assisted electrothermal-feedback transition-edge sensors (QETs). The QET signal is amplified by superconducting quantum interference devices (SQUIDs) that are thermally coupled to the cryostat's 600 mK cold stage [45]. Figure 2 shows a schematic of the ZIP channel layout. The outer charge electrode acts as a veto against events that deposit energy near the sidewalls, where higher background is expected and charge collection is more likely to be incomplete.

Data taken during the CDMS II experiment are composed of calibration (using a ^{133}Ba gamma source, or a ^{252}Cf neutron source) and WIMP search. The ^{133}Ba calibration data were used to determine the energy scale and to study various systematic effects. The ^{252}Cf calibration data were used to study detector response to NRs and act as a proxy for determining WIMP acceptance.

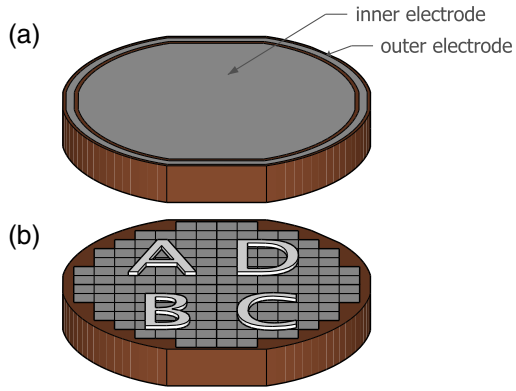

FIG. 2 (color online). a) Inner and outer electrodes for measuring the ionization signal. The inner electrode extends from the center to a radius of 34.5 mm and the outer electrode extends from a radius of 35.5 mm to just before the edge (0.5–2 mm; the diameter of the detectors is 76 mm). b) Phonon channels (QETs) A–D arranged in quadrants on the opposite side of the detector. Each phonon channel is composed of approximately 1000 TESs formed from thin films deposited onto the crystal surface and then photolithographically structured. The TESs are connected in parallel to form the QETs and each QET is read out by its own circuit containing a SQUID array.

The CDMS II front-end electronics issued experimental triggers in response to activity in either the surrounding scintillator veto or the ZIPs. For veto-triggered events, the front-end electronics required two or more veto panels to have coincident signals in excess of their hardware thresholds. ZIP-triggered events occurred when a composite phonon signal for any ZIP exceeded its preset discriminator threshold. The composite phonon signal was the analog sum of the four phonon signals from the ZIP with a 900–18 000 Hz band-pass filter applied to reduce noise-like fluctuations. During ^{133}Ba calibration runs, selective readout was employed because of the high rate; i.e. only detectors in the tower in which a ZIP trigger occurred were read out. During ^{252}Cf calibration and WIMP-search runs, all detectors were read out in response to either veto or ZIP triggers. Veto-triggered WIMP-search events were recorded for use in studies of cosmogenically induced neutron backgrounds. Each triggered event includes two charge and four phonon traces (per ZIP readout). Each trace consists of 2048 digitized amplitudes acquired at a rate of 1.25 MHz, with 512 samples prior to the trigger time.

Charge carriers moving in the electric field of the detector generate phonons with a total energy proportional to the potential difference traversed (Neganov-Luke effect [46,47]). These "Luke phonons" are typically ballistic and add to the phonon signal generated by the primary recoil. The recoil energy E_r was constructed from the total phonon energy E_p by subtracting a term proportional to the ionization-derived recoil energy E_q (or "ionization energy") to account for the Neganov-Luke effect:

$$E_r = E_p - \frac{eV}{\epsilon} E_q, \tag{1}$$

where e is the elementary charge, V is the absolute value of the operating potential of the detector, and ϵ is the average electron-hole pair creation energy. In Ge the value of ϵ is approximately 3.0 eV/pair for ERs [48]. The "ionization yield" (or yield) is defined as the ratio of ionization energy to recoil energy (E_q/E_r) and we require this quantity to be unity for ERs (see below). An NR will produce less ionization than an ER of equal recoil energy. This effect is well known [49] and provides the basis for the ZIP detector's primary method of ER/NR discrimination. For recoil energies between 10 and 100 keV in Ge, the NR ionization yield varies between 0.2 and 0.3.

Using the ^{133}Ba calibration data, the charge and phonon amplitudes were calibrated so that the energies of known gamma lines are reproduced and the yield is unity for ERs. Specifically, the charge channels were calibrated using the 356 keV line after a ∼10% correction to the ionization amplitudes to account for small systematic variations with interaction location (within the detector). We do not fully understand the origins of the systematic variation with interaction location, though it is empirically robust. One possibility is that the detectors are not neutralized uniformly by the infrared (940 nm) LED that is activated between data-taking periods to remove trapped charge. The relative phonon-channel calibration was performed by scaling the phonon-channel amplitude fractions—the amplitudes of individual channels divided by the sum of the amplitudes—to have equivalent distributions. Finally, the summed phonon energy was calibrated by requiring the ionization yield to be unity on average for ER events in the 65–100 keV region.

III. RAW DATA REDUCTION AND THE REPROCESSING

Our analysis parameters are calculated from digitized charge and phonon pulses for each ZIP detector using a set of pulse-processing algorithms. These algorithms distill timing and amplitude information from the four phonon and two charge traces (per ZIP). Surface events are rejected using timing quantities derived from the raw data, such as the rise time τ and the delay t_{del} of the largest of the four phonon pulses with respect to the faster ionization signal. The amplitude of the inner charge-channel pulse gives a measurement of E_q and the amplitude of the analog sum of the four phonon pulses gives a measurement of E_p after calibration. These energy variables are used to construct the ionization yield (y) and recoil energy (E_r) described in Eq. (1).

The relative charge-channel amplitudes (charge "partition"), relative phonon-channel amplitudes (phonon "partition"), and relative phonon pulse timing provide information about an event's position within the detector.

These additional parameters are also calculated using the output of the pulse-processing algorithms and are used for the phonon event-position-based correction and charge-derived fiducial-volume restrictions.

This section gives an overview of the most important algorithms for constructing these analysis parameters. It also explains the upgrade to the charge-pulse processing that motivated the reprocessing of this data set.

A. Parameter extraction

Timing parameters. Timing estimators are derived using an algorithm that steps along a low-pass-filtered trace to identify the pulse rise time (RT) and fall time (FT). We call this the RT-FT-walk algorithm. The traces are first filtered with a low-pass Butterworth filter [50]. Two sets of parameters are produced; one where the cutoff frequency is 50 kHz and one where it depends on the signal-to-noise of the trace. The filter removes high-frequency noise and effectively smooths the pulse for an improved determination of the RT and FT at various percentages of the pulse maximum. RT and FT information is determined by "walking" along the filtered trace starting at the maximum and identifying the times at which the respective threshold levels are reached. For example, it infers the time at which the rising pulse edge reaches 20% of the pulse's maximum amplitude. The RT-FT-walk algorithm was applied to all charge and phonon traces. The rise time τ is computed as the 10–40% time span along the rising edge of the largest of a detector's four phonon pulses using the RT-FT-walk algorithm.

Optimal filtering. A pulse-template optimal filter (OF) [51] is used to produce the best resolved energy quantities. The OF has superior energy resolution compared to pulse-integral quantities and is well suited to the analysis of small recoil energies [52]. A template for the expected pulse shape is fit to the pulse in Fourier space, deweighting the frequency bins with high noise. The frequency deweighting is done for each individual data "series"—a data-taking block normally lasting between 10 and 12 h—using noise power spectral densities (PSDs). The PSD is constructed from randomly triggered traces taken before the series to sample the noise environment. Phonon pulse templates are two-exponential functional forms, with rise- and fall-time parameters tuned to match individual detectors by fitting to an average pulse. Charge pulse templates were produced empirically by averaging normalized data traces. This fitting procedure is done for all possible pulse template delays and the best-fit delay is chosen.

A single-pulse-template OF is performed on each phonon pulse separately and on the sum of a detector's four phonon traces. For charge pulses, to account for crosstalk between the inner and outer channels, the two pulses are fit simultaneously with a crosstalk-correcting OF (OFX) described in more detail below. During the OF fit an array of best-fit amplitudes is produced that corresponds to each possible delay of the template with respect to the experimental pulse. The maximum such amplitude in a preselected delay window is chosen and its time defines the delay quantity. For an OF using a single pulse template this maximum amplitude choice also has the lowest χ^2 in the preselected window. The OF amplitude for the summed phonon trace gives E_p after calibration and the inner charge amplitude from the OFX procedure gives E_q after calibration. The charge-to-phonon delay t_{del} is determined from the difference between the OFX charge delay and the 20% crossing of the largest phonon signal as determined by the RT-FT-walk algorithm. The delay is computed as follows:

$$t_{\mathrm{del}} = t_{p20} - t_{\mathrm{OFX}}, \tag{2}$$

with t_{OFX} being the OFX ionization delay relative to the global trigger time and t_{p20} being the 20% crossing time of the largest phonon signal relative to the global trigger.

B. Parameter corrections

Phonon position correction. The phonon sensor response is highly position dependent [53]. In order to optimize the derived phonon variables, a position correction was used to modify energy, timing, and yield quantities by normalizing to the mean of nearby events. We first defined averaging neighborhoods using a five-dimensional metric that included total phonon energy, two relative phonon delay parameters, and two phonon energy partition parameters [54]. For each parameter to be corrected, a lookup table containing the neighborhood averages for each five-dimensional bin was then constructed using bulk ER events confirmed to be of good quality from ^{133}Ba calibration. To apply the correction we created a corrected version (v_c) of a given parameter (v) as in Eq. (3):

$$v_c = \frac{v}{\langle v \rangle_{\mathrm{bin}}} \langle v \rangle_{\mathrm{global}}, \tag{3}$$

where the subscript "global" refers to averaging over the whole calibration data set, and "bin" refers to averaging over one neighborhood. After the lookup table was applied to the ^{133}Ba calibration data, the selection of bulk ERs was refined to create the final correction table, which was then applied to the WIMP-search data. The final energy, timing and yield quantities were made more uniform across the detector for bulk events by using this procedure, thus improving the rejection of surface events.

Charge crosstalk. Charge signal quantities use the OFX algorithm to account for crosstalk. Using separate pulse-template OFs for the inner and outer electrodes, a single delay was chosen. In the original analysis of our data set [33], this delay corresponded to the delay that made the sum of the two OF amplitudes maximal. While this is likely to be very close to the delay that minimizes the χ^2 of the fit,

it is not guaranteed because of the combined fitting of the inner and outer electrodes.

C. Reanalysis motivation

After finalizing the first analysis of this data set in 2009 [33] we noticed that one of the WIMP candidate events had an OFX delay value that did not correspond to a global minimum in the χ^2 of the fit (see Fig. 3). This issue was one of the main reasons for proceeding with a reanalysis.

The reason for implementing the maximum-amplitude method instead of a full χ^2 minimization in the original analysis was to save computing time; a global trigger issued by one detector forces the readout of all detectors, giving a substantial number of traces with near-zero amplitudes that need not be processed with the time-consuming χ^2 minimization. The result of using this maximum-amplitude method is to smear the ionization-to-phonon delay distributions slightly, which can cause additional background events to leak past the timing cuts. This delay smearing affects lower-ionization events more than higher-ionization events. In particular, NRs that deposit energy in a single detector ("single scatters") are more susceptible than the (higher-ionization) low-yield ERs used to quantify the expected leakage of surface events into the signal region.

The OFX inaccuracy made only a small contribution to the previously published limit, and background estimates were adjusted upward in the original result to account for the resulting larger uncertainties at low energies [33].

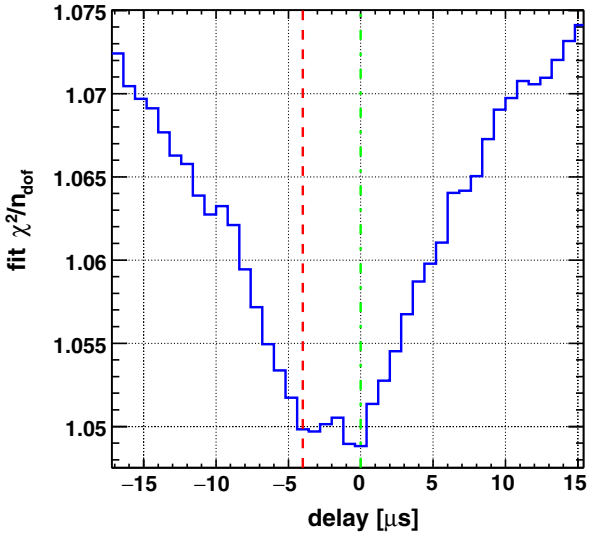

FIG. 3 (color online). The OFX χ^2 as a function of delay for the T3Z4 WIMP candidate from the original analysis [33]. The delay chosen by the original ionization fit to this event (red dashed line) is not a global minimum in χ^2; rather it is displaced ∼4 μs from the global minimum (green dot-dashed line). While this small error in the inferred delay for this and other events did not affect the measured energy significantly (a ∼2% decrease), it caused an error in the surface-event-rejection timing parameter for low-energy events.

Nevertheless, the number and character of the candidate events provides useful information on the possibility of a signal. It is very likely that the candidate event featured in Fig. 3 would have been removed by the timing cut in the original work had the ionization delay at the global minimum of the χ^2 been chosen, but using the improved OFX procedure also has the potential to cause previously excluded events to become WIMP candidates.

For the reasons stated above, the data were reprocessed, selecting the global minimum of the χ^2 in the OFX algorithm for most ionization pulses, rather than the maximum-amplitude method. Because of the large number of traces in the raw data consistent with noise, traces with pulses corresponding to charge energies below a detector-dependent threshold (0.94 $\mathrm{keV_{ee}}$ [38] on average across the 14 detectors used in this work) were still processed with the maximum-amplitude method in order to save processing time. This has no effect on the results presented here because this energy is below our lowest analysis threshold.

IV. DATA SELECTION AND EFFICIENCIES

Once the data set was calibrated and position corrected, we created several selection criteria (or "cuts") to produce the cleanest signal-region sample possible. Since the rejection of nonsignal events is typically not perfect, a signal event retention efficiency was computed for each cut. The cuts and efficiencies are covered in this section, starting with the efficiency for the trigger—a selection criterion that is made in hardware before the events are recorded. The result is a signal-region sample corresponding to a well-known exposure.

A trigger efficiency for each detector was determined as a function of phonon energy and converted to a function of recoil energy using our measured NR ionization yield from ^{252}Cf data. A given detector's trigger efficiency was calculated using all WIMP-search events in which another detector caused an experimental trigger. When the global trigger initiates a readout of all the detectors, other delayed instances where phonon pulses were in excess of the corresponding discriminator thresholds were recorded into a logical buffer. Regardless of the content of these trigger records, for each event and detector the optimal-filtering techniques described in Sec. II were used to reconstruct the total phonon energy (E_p) from Eq. (1). The trigger efficiency curve is then the ratio of two recoil-energy spectra: the spectrum of events with a phonon trigger in both the detector in question and another detector divided by the spectrum of events with a phonon trigger in another detector. As shown in Fig. 4—combined across the 14 Ge detectors considered here—the trigger efficiency is ∼100% for recoil energies above our standard analysis threshold of 10 keV. Note that the extended analysis described in Sec. V D requires the trigger efficiency down to ∼5 keV.

Events above the trigger threshold were subjected to five classes of cuts used to isolate high-quality signal candidates

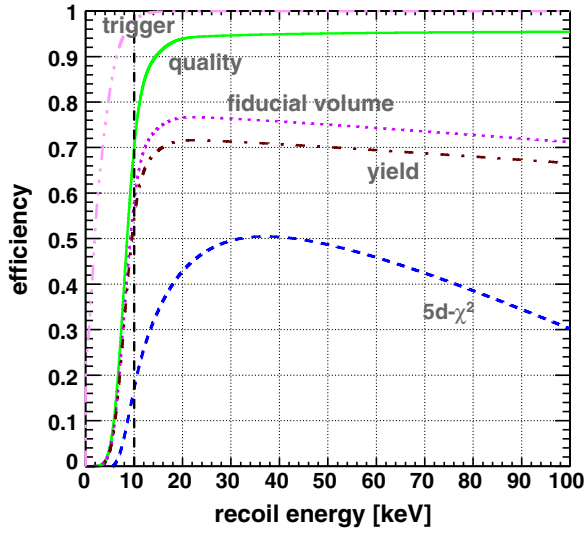

FIG. 4 (color online). Detection efficiency combined across all detectors as a function of energy for different classes of cuts. The curves show the total efficiency as more cuts are added beyond the hardware trigger (pink triple-dot-dashed): event-level data-quality cuts (green solid), ionization-based fiducial-volume cut (magenta dotted), ionization-yield cut (maroon dot-dashed), and 5d-χ^2 (see Sec. V C) phonon timing cut (blue dashed). The falloff of the data-quality cut efficiency below ~20 keV is due to the interplay between the ionization threshold and the requirement that the ionization yield be 3σ below the ER band (see main text). The vertical black dashed line is our standard 10 keV analysis threshold.

in the WIMP-search data: cuts that remove time periods of reduced overall data quality; event-level data-quality cuts; an ionization-based fiducial-volume cut to reject events near the detector sidewall; an ionization-yield cut; and one of three phonon timing cuts. Cuts that remove time periods cause a loss of experimental live time because events are removed uniformly for all detectors and in all kinematic variables. After the live-time cut, the total remaining live time for each detector was computed and stored. All other cuts cause reductions in NR detection efficiency, some of which vary significantly as a function of recoil energy. We computed these "efficiency functions" and applied them to each detector in conjunction with the live time to compute the final exposures.

The NR detection efficiency functions were estimated in bins of recoil energy. Well-motivated functional forms were fit to the bin-wise estimates, with the best-fit results shown in Fig. 4. Most cuts have little effect on the acceptance of nuclear recoils. The ionization-based fiducial-volume cut and the phonon timing cuts cause the greatest loss of signal acceptance. Of the three timing cuts described in Sec. V, use of the "5d-χ^2" timing cut results in the highest final acceptance above 10 keV, about 50% at ~35 keV. The 5d-χ^2 timing-cut efficiency is shown in Fig. 4 as an example while the other timing-cut efficiencies are detailed in Sec. V E.

A. Live-time cuts

Live time was removed during periods with disabled readout channels, poor detector neutralization (characterized by increased levels of charge trapping in the crystal bulk [52]), decreased resolution, improper experimental configurations, and trigger anomalies that consist of isolated bursts of events or incorrect phonon trigger threshold. The Soudan Underground Laboratory also houses a neutrino detector, MINOS, to measure properties of the "NuMI" neutrino beam originating from Fermi National Accelerator Laboratory [55]. While it is very unlikely for CDMS to observe any beam-induced events, the loss of live time incurred by removing all time periods coincident with a NuMI beam spill is negligible. The NuMI neutrino-beam cut is implemented as a restriction on the live time, removing events within 60 μs of the arrival of the neutrino beam's 10 μs spills. After application of these cuts, 612 kg days of total exposure remain. We define this as our "raw exposure." Out of a total of 36% loss of live time (64% data-taking efficiency) the largest contributors were bad environmental configurations (~15%), failed KS tests (~8%), cryocooler noise (~6%), poor phonon reconstruction (~4%), and fundamental hardware failures (~3%). Bad environmental configurations can consist of many effects including trigger bursts, high charge noise, or insufficient LED flashing.

B. Quality cuts

The event-level class of quality cuts consists of several components. A "glitch" cut removes events that have phonon pulses resembling electronic noise in the phonon readout chain. These events are typically correlated across multiple detectors and are characterized by phonon pulses with fall times shorter than the time scale expected for phonon dissipation. Such events are less likely to appear in the ionization readout chain; consequently, they are effectively removed with a cut that rejects events in which the phonon pulse multiplicity is significantly larger than the ionization pulse multiplicity [56]. The muon-veto cut uses the 2 in. thick scintillator panels that surround the CDMS II experiment and the following two rejection criteria: an event was removed if 1) a ZIP event is associated with a muon-like energy deposition (0.58 V or ~3.8 MeV deposited) in any veto panel occurring between 185 μs before and 20 μs after the ZIP trigger time, or 2) there is any veto activity above the scintillator-panel hardware threshold (~0.23 V) and within the 50 μs before a ZIP trigger. Both criteria are used for the muon-veto cut because it makes the cut stronger and has only about a 2% efficiency loss across all recoil energies. Finally, because WIMPs will not interact in more than one detector within a given event, we defined a "single-scatter" cut to select events involving a single ZIP detector as follows: 1) the phonon signal must be greater than six standard deviations above the mean electronic-noise level in the detector under consideration;

and 2) the signal in all other detectors must be within four standard deviations of the means of their respective noise distributions. Ionization channels were used for multiple-scatter rejection for those detectors with degraded phonon channel performance. Thus, Ge and Si detectors that are not part of the WIMP-search exposure were still live with respect to identification and rejection of multiple-scatter events. The single-scatter cut efficiency for each detector was estimated from the fraction of randomly triggered events (i.e., electronic noise) that satisfy criterion 2). The combined efficiency of the glitch, muon-veto and singles cuts varies by detector and over time, and ranges from 96% to 98%. Another aspect of the singles cut is its use to select certain samples from calibration data. For example, multiple-scatter events that have their secondary scatter in the detector above or below the triggering detector are said to be "face tagged." For these events the primary recoil is biased toward the direction facing the multiples tag. When using the multiples in background estimations, separating the events by face helps decrease the systematic uncertainties (see Sec. VII A). Sometimes events with multiples toward the phonon readout side are called "phonon-side" and those with multiples toward the charge readout side are called "charge-side."

Some quality cuts depend explicitly on the kinematic variables. One of these is an ionization threshold cut, which requires events to have reconstructed ionization signals greater than 4.5 standard deviations above the mean noise level. This cut removes nearly all events with zero charge collected (those from very near the side walls), resulting in <0.1 of such events over the whole exposure. A charge-pulse reconstruction-quality cut was also defined, requiring the χ^2 value of the OFX fit to be less than an energy-dependent threshold. This cut selects events with high-quality charge energy estimators, suppressing those with excess electronic noise or the occurrence of multiple pulses within a single event trace (referred to as "pile-up"). Its efficiency was measured as a function of charge energy using ^{133}Ba calibration data and translated into recoil energy using the average NR ionization yield measured from ^{252}Cf calibration. Above $\sim$20 keV$_{ee}$ [38] the efficiency is constant and $>99\%$. It decreases slightly at lower recoil energies.

Charge collection is reduced near the cylindrical walls of the detector, causing lower ionization yield and thus poor NR to ER discrimination. The ionization-based fiducial-volume cut accepts only events with an outer electrode signal consistent with noise. The efficiency of this cut (see Fig. 4) was estimated using the ^{252}Cf calibration data, including a small correction ($\sim$13% maximum across the energy range) accounting for residual leakage of ERs into the NR signal region in these data. Another $\sim$5% correction was applied across the whole energy range to account for detector self-shielding to neutrons and multiple scattering; this correction was based on a Monte Carlo simulation of neutron scattering.

C. Yield cut

An energy-dependent cut on ionization yield is used as the primary method for discriminating NRs from ERs. An NR "band" was derived for each detector by fitting the distribution of NR yields in ^{252}Cf calibration with a Gaussian hypothesis in bins of recoil energy. The collections of best-fit Gaussian means and widths were then fit with energy-dependent functional forms, giving smooth parametrizations versus recoil energy of the average yield and the yield resolution for NRs. The functional form for the means was inspired by the Lindhard theory [57] ($y = a \cdot E_r^b$, where a and b are fitted parameters), whereas the widths are fit to a power law below a fitted energy threshold and a constant above [58]. ER bands were similarly constructed from ^{133}Ba calibration. The primary ionization-yield cut requires that events be located within the $\pm 2\sigma$ width of the NR band. By construction, the selection efficiency is $\sim$95% and roughly constant with energy (see Fig. 4). Variations in detector response over the course of the WIMP search caused slight variations in each detector's NR and ER bands. Consequently, the bands depend on both detector and time. The time variation is represented by widths of the band lines shown in Fig. 5, where they are plotted with the ^{252}Cf data from which the NR bands are derived.

To prevent ERs from entering the signal region at low recoil energy where the ER and NR bands overlap (see Fig. 5), the yield-based discrimination is refined to include a requirement that candidate events lie at least 3σ below the

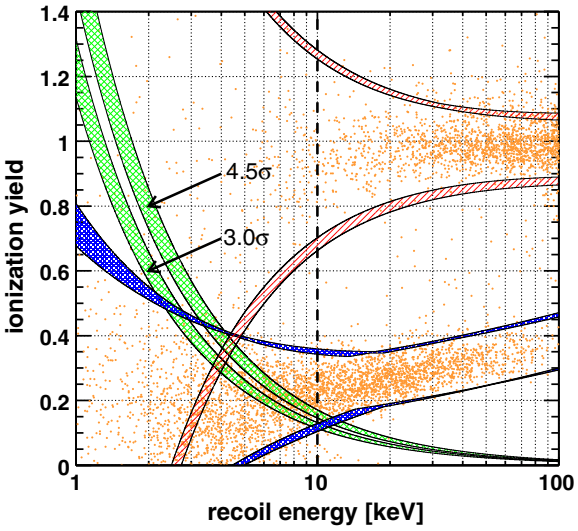

FIG. 5 (color online). ER and NR bands defined in the plane of yield versus recoil energy for a representative detector (T1Z2). The ER band mean $\pm 3\sigma$ curves (red hatched), NR band mean $\pm 2\sigma$ curves (blue fine cross-hatched), ionization threshold 3.0σ and 4.5σ curves (green coarse cross-hatched), and the 10 keV threshold line (black dashed) are shown superimposed onto ^{252}Cf data (points). The widths of the bands represent the time-period variation of the fits that are used to define them.

mean of the ER band (see Sec. IV D). This condition and the ionization threshold have the greatest impact on the overall NR detection efficiency at low energies. The efficiencies for these two cuts are 100% for recoil energies greater than $\sim 15-25$ keV (depending on the detector) and decrease rapidly to zero for lower energies. This behavior is illustrated in Fig. 4, where the efficiency of these two cuts is shown combined with the other event-level quality cuts.

D. Data regions

To assess the effectiveness of the timing cuts defined in Sec. V, several standard data regions in the nontiming variables were defined. This terminology will be used throughout the rest of this work to describe data samples used for timing-cut tuning and sideband-style background estimations. All of the event samples include the data-quality and fiducial-volume restrictions. Further, they include the requirement that events have charge energies greater than 4.5 standard deviations above the mean electronic-noise level.

(i) **Nuclear-recoil single scatter (NRSS).** Events that are below the ER band mean -3σ line, within the NR band mean $\pm 2\sigma$ lines, and are single scatters. The portion of the NRSS events that pass the timing cut and are in the range of 10–100 keV make up the WIMP signal region. The 5d-χ^2 timing cut uses a slightly modified signal region in that the width of the NR band is optimized. We use the term NRSS there as well, leaving the precise width of the NR band to be determined from context.

(ii) **Nuclear-recoil multiple scatter (NRMS).** Events that are below the ER band mean -3σ line, within the NR band mean $\pm 2\sigma$ lines, and are not single scatters.

(iii) **Wide-band (WB).** Events that are below the ER band mean -5σ line, and above the NR band mean +2σ line.

(iv) **Wide-band multiple scatter (WBMS).** Events that are below the ER band mean -5σ line, above the NR band mean $+2\sigma$ line, and are not single scatters. These events are a good representation of surface events.

V. PHONON TIMING DISCRIMINATION

ZIP detectors have an excellent ability to discriminate NRs from ERs if the energy depositions occur away from the surfaces of the detector. But background surface events can populate the NR band, despite being ER in nature, since they can have reduced ionization yield. We remove surface events from our WIMP candidate sample using the timing characteristics of the phonon signals. A small number of surface events, however, can survive into the signal region. We call these leakage events. The definition of the timing cut affects the surface-event leakage and the total exposure (through the NR acceptance), so a crucial element in the timing-cut construction is tuning for optimal WIMP-detection sensitivity. Three timing-cut constructions are reviewed in this section.

Having three independent methods for surface-event rejection gives a handle on the systematic uncertainty of the leakage estimates. The WIMP limits for these three realizations of surface-event rejection and sensitivity maximization are presented in Sec. VIII. Table I gives a summary of the different timing parameters used for each timing cut construction: the "classic," "neural-network," and "5d-χ^2" analyses. The choice of parameters used in particular timing-cut constructions is explained in the following sections.

Each of the timing cuts was optimized to produce the best expected sensitivity to WIMPs given the expected leakage. Since we do not know the WIMP mass, a "target" value is chosen for each analysis (60 GeV/c^2 for most analyses in this work) and the expected sensitivity is maximized given that WIMP mass. The spectrum-averaged exposure (SAE) is a way to quantify the amount of the raw exposure (MT = detector Mass × live Time) that is utilized toward the WIMP search over the analysis energy range, given a WIMP recoil spectrum for mass m_χ of $f(E_r; m_\chi)$. The SAE is computed as follows:

$$\mathrm{SAE}(m_\chi, E_l, E_h) = \mathrm{MT}\frac{\int_{E_l}^{E_h} dE_r \epsilon(E_r) f(E_r; m_\chi)}{\int_{E_l}^{E_h} dE_r f(E_r; m_\chi)}, \quad (4)$$

where E_r is the recoil energy, E_l (E_h) is the lower (upper) signal-region energy limit, and $\epsilon(E_r)$ is the cumulative signal acceptance efficiency for all cuts at a recoil energy E_r. Note that the SAE is equal to the raw exposure only when the analysis efficiency is unity over the entire energy range and that only SAEs with the same WIMP-mass assumptions and signal-region energy range are strictly comparable. Sometimes the right-hand side of Eq. (4) with MT divided out is called the spectrum-averaged efficiency. The SAE is computed on a detector-by-detector basis and then summed in the final analysis.

TABLE I. Brief description of each of the phonon timing quantities used in this work. The abbreviation "VF" indicates the use of variable-frequency filtering prior to the application of the RT-FT-walk algorithm. "CF" indicates a constant (50 kHz) filter prior to that algorithm (see Sec. III A). Under "Analysis," "NN" refers to the neural-network timing analysis.

Quantity	Description	Analysis
τ	VF phonon rise time	NN, 5d-χ^2
t_{del}	VF phonon delay	NN, 5d-χ^2
$\tilde{\tau}$	CF phonon rise time	Classic, 5d-χ^2
$\tilde{t}_{\mathrm{del}}$	CF phonon delay	Classic, 5d-χ^2
$\tilde{\tau}_{4070}$	CF phonon 40–70% rise time	5d-χ^2
$\tilde{w}$	CF phonon pulse width	NN
P_{5070}	phonon 50–70 kHz power	NN

Before looking at the events in the final signal region (see Sec. VI on "unblinding") we used the expected leakage and the SAE of each timing cut optimization to calculate the expected sensitivity. The expected sensitivity is computed by using the expected leakage and calculating the upper limit of counts at the 90% C.L. This is normalized by the SAE to produce the lowest WIMP rate the experiment is sensitive to. For the 10 keV threshold analysis the 5d-χ^2 timing cut had the best sensitivity, while our lower-threshold analysis showed the classic method to have the best sensitivity. The main results of this work are therefore the limits of the 5d-χ^2 analysis for WIMP masses above 11.3 GeV/c^2, and the limits of the classic method for WIMP masses below 11.3 GeV/c^2.

A. Classic timing analysis

The phonon timing cut strategy that was used in the original analysis of these, as well as earlier CDMS data [33,36,59] was also used in our reanalysis and provides a point of comparison between the two.

Our "classic" timing parameter is defined as the sum of two quantities: the delay ($t_{\rm del}$) and the 10–40% rise time (τ), both derived from the most energetic phonon signal among the four sensors (see Sec. III). The sum is approximately the optimal combination of these two variables, as can be seen in Fig. 6. A timing cut is defined as a set of detector-dependent thresholds on the distributions of this parameter, below which all events are rejected. The thresholds were determined by an optimization scheme that approximately maximizes the sensitivity to a WIMP with a mass of 60 GeV/c^2. Practically, this was accomplished by maximizing the WIMP-search exposure (as measured with ^{252}Cf NRs) while keeping the total leakage approximately equal to a "target" leakage of ~0.5 events. This approximately maximized the 60 GeV/c^2 WIMP sensitivity while keeping the total expected leakage well under one event [60].

The expected surface-event leakage was estimated from representative ^{133}Ba calibration and sidebands in the WIMP-search data that are insensitive to WIMPs. The surface-event background estimates for the three timing-cut strategies are described in detail in Sec. VII A. Although the quality cuts remove most unusual events, data-reconstruction artifacts occasionally result in events with extreme kinematic quantities ("outliers"). To prevent such outliers from skewing the timing-cut optimization, a consistency cut rejects events for which $\tau + t_{\rm del}$ is greater than 32 μs or τ-$t_{\rm del}$ falls outside the 0.5% and 99.5% quantiles of the combined ^{133}Ba and ^{252}Cf data sets. Figure 6 shows the classic timing cut in the delay versus rise-time plane, and Fig. 7 shows the cut in the yield versus timing-parameter plane for an example detector [61]. Applying this timing cut results in a total SAE summed over detectors of 220 kg days between 10 and 100 keV for a 60 GeV/c^2 WIMP and an expected surface-event leakage of $0.64\,(+0.17-0.15)_{\rm stat}$ events, calculated after unblinding. The post-unblinding calculation is generally more accurate because it makes use of the previously sequestered

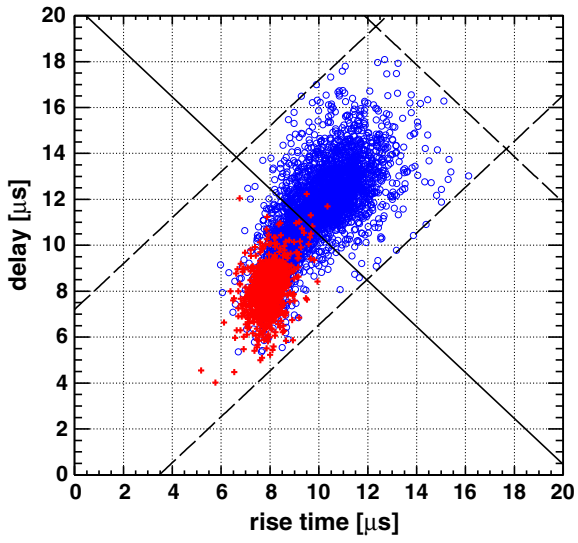

FIG. 6 (color online). Classic timing cut in the delay versus rise-time plane for a representative detector (T1Z5). ^{252}Cf NRSS and NRMS events (blue open circles) and ^{133}Ba WBMS events (red crosses) are shown. Accepted events lie within the "consistency" region (black dashed lines) and to the upper right of the discrimination cut (black solid line). Considering the ^{133}Ba WBMS events (red crosses), 2381 events fail the timing cut and four events pass.

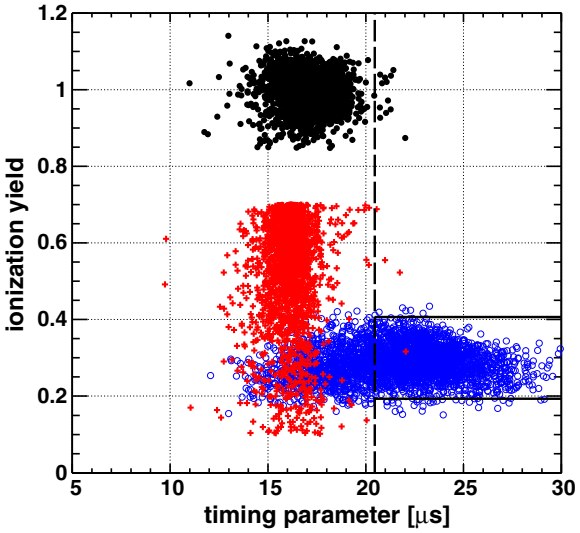

FIG. 7 (color online). Classic timing cut in the ionization-yield versus timing-parameter plane for a representative detector (T1Z5). ^{252}Cf NRSS and NRMS events (blue open circles), ^{133}Ba WBMS events (red crosses), and ^{133}Ba events in the ER $\pm 2\sigma$ band (black filled circles) are shown. Accepted events lie to the right of the timing parameter line (black dashed line) and in the NR band (black solid lines). Considering the ^{133}Ba WBMS events (red crosses), 2381 events fail the timing cut and four events pass.

(see Sec. VI) NR single scatters that failed the timing cut (see Sec. VII).

B. Neural-network timing analysis

A neural-network technique was used to develop a timing cut using four timing parameters: the previously defined phonon delay $t_{\rm del}$ (i) and rise time τ (ii); the phonon pulse width $\tilde{w}$ (iii), defined as the time difference between the 80% points on the rising and falling edges of the largest-amplitude phonon pulse; and the spectral power of the largest phonon pulse P_{5070} (iv), integrated between 50 and 70 kHz [62]. These parameters were chosen because they showed the most promising discrimination in their one-dimensional distributions.

These four variables were fed into a principal component analysis [63]. Principal component analysis is a statistical method for determining a unitary transformation that takes N possibly correlated input vectors and returns N output vectors that are linear combinations of the input vectors ($N = 4$ in this case). The output vectors are ordered by their statistical variance, so that the output vector with the ith-highest variance is called the ith principal component. Since the input vectors can have different characteristic scales and are dimensional, the input vectors were normalized to zero mean and unity variance so that the ordering of statistical variances of the output vectors is meaningful in an absolute sense.

Neural-network computational complexity scales poorly with the number of input parameters. Therefore, only the first two principal components (i.e., those with the highest variance) were selected as inputs for the neural network. Given input parameters with similar intrinsic resolution and physical relevance, the high-variance combinations will be those that maximally separate the distinct populations (i.e., NRs and ER surface events). Principal components were selected separately for each detector and for several bins of time spanning the WIMP-search data set. The latter is necessary to capture changes in detector performance caused by variations in operating conditions. The principal component rotation showed that all four timing parameters contribute significantly to the first and second principal components in most cases. This generally indicates that the use of the extra parameters (as compared to the classic analysis) is beneficial even though in the end the sensitivity change is not dramatic (see Sec. VIII A).

The neural network that was used is a multilayer perceptron with one hidden layer, 30 neurons, and a logistic sigmoid activation function. The NETLAB package [64] for MATLAB was used to perform this analysis. Training samples for surface events and NRs were selected from the ^{133}Ba and ^{252}Cf calibration data, respectively. Events from the NR training sample were assigned a target output value of 1, while surface events were assigned a target value of 0. Data were sorted into two bins of recoil energy, above and below 30 keV, in order to take the energy dependence of the timing parameters into account. Finer energy binning was not possible because of small statistics in the training samples.

Separate neural networks were trained for each combination of detector, time period, and energy bin using the standard back-propagation-of-errors training algorithm [64]. Once the neural networks were trained, they assigned a numerical value to each event in the range 0–1. An output value close to 1 (0) corresponds to events of NR-like (surface-event-like) character. The distributions of this output parameter for the calibration data, as seen in Fig. 8, were then used to set a threshold for each detector, time period, and energy bin.

The thresholds were set such that the WIMP-search exposure is maximized using a target surface-event leakage of 0.5 events. As in the classic analysis, this target leakage approximately maximized the 60 GeV/c^2 WIMP sensitivity and the same optimization procedure was used. Following optimization, the total SAE for a 60 GeV/c^2 WIMP is about 216 kg days, with an expected leakage of $0.87\,(+0.24-0.21)_{\rm stat}$ events. Similar to the leakage estimate for the classic timing cut, this expected leakage was estimated after unblinding for better accuracy (see Sec. VII).

C. 5d-χ^2 timing analysis

The 5d-χ^2 surface-event rejection [65] was implemented by differentiating events based on a goodness of fit to two event-type hypotheses [66,67]: $\chi^2_{\rm N}$ for NR, and $\chi^2_{\rm B}$ for surface events. Five timing quantities were used to form each χ^2 value. Three of the quantities are measures of rise time for the largest-amplitude phonon channel: two based on the 10–40% rise time (τ and $\tilde{\tau}$); and one based on the 40–70% rise time ($\tilde{\tau}_{4070}$). The remaining two quantities correspond to the delay of the phonon pulse relative to the prompt charge pulse: one computed using a variable and one a constant-frequency RT-FT walk ($t_{\rm del}$ and $\tilde{t}_{\rm del}$). The inclusion of different measures of the same physical quantities (delay and rise time here) increases the robustness of the χ^2 value and is more effective at identifying outliers. Therefore, the delay and rise-time parameters with good one-dimensional discrimination and the least redundancy (correlation) were chosen.

Event samples of neutrons and surface events taken from calibration data were used to constrain the timing-quantity distributions for each event type. For each detector, calibration data were separated into neutron, charge-side surface-event, and phonon-side surface-event samples. The energy-dependent means, $\boldsymbol{\mu}(E_r;\alpha)$—a vector of the timing-quantity distribution means for each event type α—were then fit to the empirically motivated functional form

$$\boldsymbol{\mu}(E_r;\alpha) = \boldsymbol{a}_1(\alpha) + \boldsymbol{a}_2(\alpha)E_r^2 + \boldsymbol{a}_3(\alpha)\sqrt{E_r}, \qquad (5)$$

where the $\boldsymbol{a}_i(\alpha)$ are free parameters for each timing quantity (the vector indices) and for particle type α. The $\sqrt{E_r}$ term is observed to improve the fit. The covariance matrix $\boldsymbol{\sigma}(E_r;\alpha)$ was similarly fit using

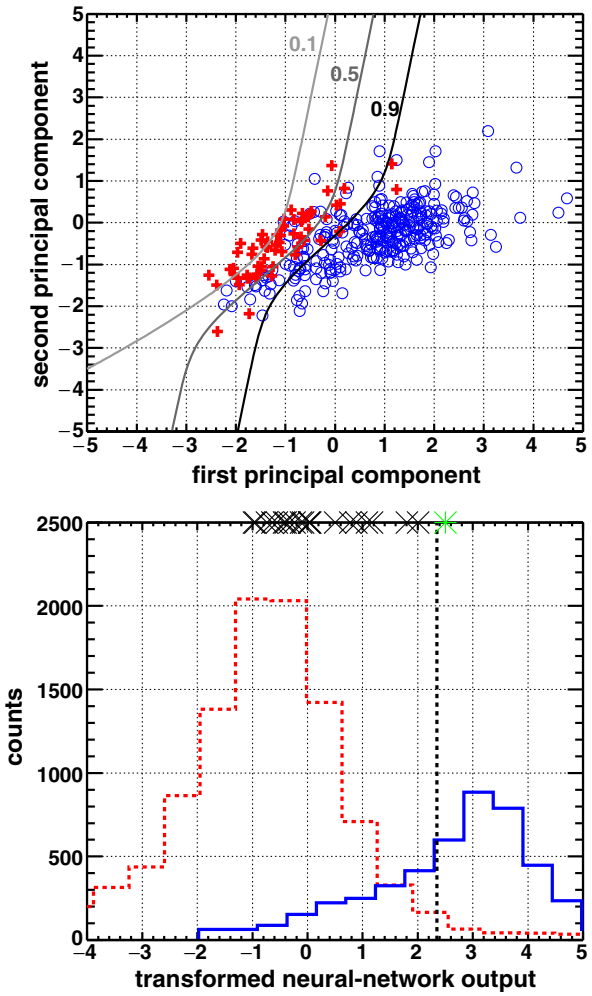

FIG. 8 (color online). Neural-network training distributions of a representative detector (T1Z5), for the low-energy neural-network bin (<30 keV). (Top panel) Contours of constant neural-network output (grayscale solid curves; see text) in the plane of the first two principal components. ^{252}Cf NRSS and NRMS events (blue open circles) and ^{133}Ba WBMS events (red crosses) are also shown. (Bottom panel) Distributions of the "transformed" neural-network output: the distribution of NRs from the ^{252}Cf data mentioned above (blue solid); and the surface-event distribution from the ^{133}Ba data mentioned above (red dashed). The cut threshold (vertical black dashed line) with the WIMP-search data passing (green asterisk) and failing (black × 's) the timing cut are also plotted along the top of the plot. The transformed neural network is used to make the distribution separation more visible; it is computed by using the inverse of the neuron response function: ϕ: $(-\infty, \infty) \to (0, 1)$ with $\phi(x) = 1/(1 + e^{-x})$.

$$\boldsymbol{\sigma}^2(E_r;\alpha) = \boldsymbol{b}_1(\alpha) + \frac{\boldsymbol{b}_2(\alpha)}{E_r^2}, \tag{6}$$

where the $\boldsymbol{b}_i(\alpha)$ are matrices of the free parameters for each pair of timing quantities and particle type α. The functional form of the variance was motivated by noting that in a simple model of a pulse with a linear rise but constant rise time, the probability for a noise fluctuation before the pulse rises above the noise is inversely proportional to the slope, and therefore is proportional to the inverse of the amplitude (energy).

The χ^2_α was then formed for every event according to the following formula:

$$\chi^2_\alpha(E_r) = (\boldsymbol{\xi} - \boldsymbol{\mu})^T \cdot (\boldsymbol{\sigma}^2)^{-1} \cdot (\boldsymbol{\xi} - \boldsymbol{\mu}). \tag{7}$$

Here $\boldsymbol{\xi}$ is the vector embedding the five timing variables for each event and the dependence on E_r and α has been left implicit on the right-hand side.

The surface-event goodness-of-fit variable χ^2_{B} was constructed for each event by the definition

$$\chi^2_{\mathrm{B}} \equiv \min(\chi^2_p, \chi^2_q), \tag{8}$$

where χ^2_q and χ^2_p are the charge-side surface-event and phonon-side surface-event goodness-of-fit variables respectively.

Two restrictions were set in the plane of χ^2_{B} versus χ^2_{N} that together complete the definition of the 5d-χ^2 surface-event rejection cut (see Fig. 9). First the potential WIMP events were required to have $\chi^2_{\mathrm{N}} \leq c_i$, where c_i is a value for the ith detector, set by requiring that 90% of the calibration-data neutrons pass the cut. To distinguish potential signal events from surface events, it was required that $\chi^2_{\mathrm{B}} - \chi^2_{\mathrm{N}} \geq \eta_i(e)$ where the index i indicates the detector number and the parameter e indicates the event's energy bin (10–20 keV, 20–30 keV, or 30–100 keV).

We parametrize—using adjustable parameters t and b—the ionization-yield (y) restriction as

$$\mu_{nr} - b\sigma_{nr} \leq y \leq \mu_{nr} + t\sigma_{nr}, \tag{9}$$

where $\mu_{nr}(E_r)$ and $\sigma_{nr}(E_r)$ are the energy-dependent mean and standard deviation of the ionization yield for NRs, as found using neutron calibration data. The parameters t and b were required to be the same for all detectors and energy bins. The values $\eta_i(e)$, t, and b were determined by a simultaneous optimization for all detectors and energy bins that maximizes the total SAE for 60 GeV/c^2 WIMPs.

Optimization of the 5d-χ^2 timing cut and the NR band definition was based on requiring the best overall expected sensitivity. For a given timing cut (the set $\{\eta_i\}$) and NR band definition, the expected sensitivity is constructed by dividing the 90% Poisson upper limit on the expected leakage by the SAE. For an individual detector we denote the leakage as $\mathcal{L}_i(\eta_i)$ and the SAE as $\mathcal{S}_i(\eta_i)$. These are smooth functions computed by fitting leakage and exposure evaluations at discrete η_i using ^{133}Ba calibration data.

Because the cut is defined such that decreasing η_i will loosen the restriction, both the leakage and the SAE for each detector are monotonically decreasing—leading to the condition that the slopes $d\mathcal{S}_i/d\mathcal{L}_i$ for the optimum cut are equal. If not, a unit increase in the leakage of a detector with larger slope could be offset by a unit decrease in a detector

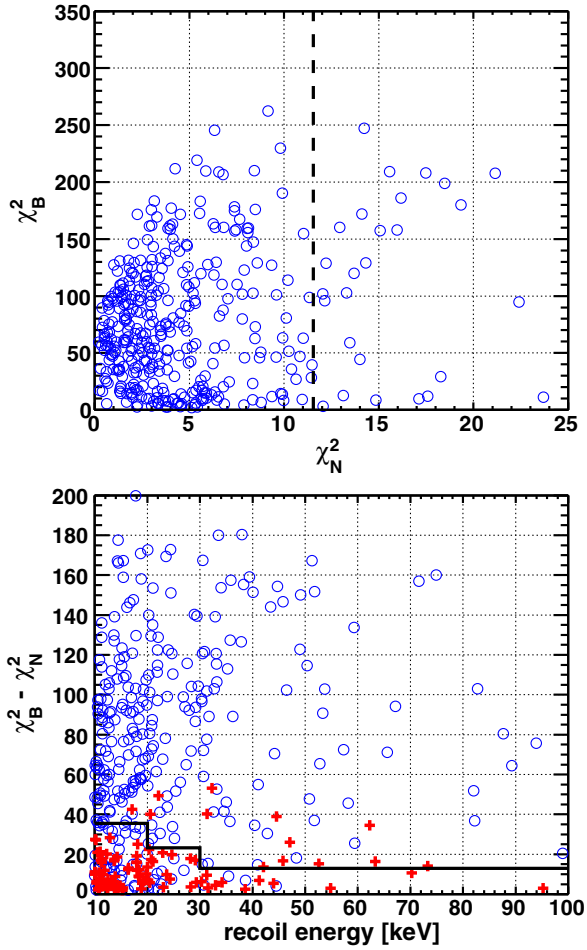

FIG. 9 (color online). Distributions of calibration data in the 5d-χ^2 parameters for a representative detector (T1Z2). (Top panel) ^{252}Cf events in the NR $\pm 2\sigma$ band (blue open circles) are shown with the consistency cut that retains 90% of neutrons (vertical black dashed line) in the χ^2_B versus χ^2_N plane. (Bottom panel) Events passing the consistency cut—NRs from ^{252}Cf data (blue open circles) and surface events from ^{133}Ba data (red crosses)—in the $\chi^2_B - \chi^2_N$ versus recoil-energy plane. The energy-dependent 5d-χ^2 timing cut is also shown (black solid line) and events above the line pass the cut. Note the cut is tighter at low energies and looser at higher energies.

with a smaller slope with a net increase in exposure, improving the sensitivity. The timing cut optimization was done with respect to this slope, which parametrizes the $\{\eta_i\}$ uniquely.

For the optimum set of timing parameters $\{\eta_i\}$ the NR band definition is selected by choosing the values of t and b that optimize the overall expected sensitivity.

The yield and timing cuts that optimize the expected sensitivity for a 60 GeV/c^2 WIMP produced an asymmetric NR band cut with $b = -1.9$ and $t = 1.8$. The sensitivity optimization gives a total expected leakage of 0.5 events and a total SAE of 250 kg days given a WIMP mass of 60 GeV/c^2. The estimated leakage after unblinding is $1.19(+0.23 - 0.21)_{\text{stat}}$ events.

D. Extended analyses

There has been growing interest in low-mass WIMP searches because of some intriguing published results [39,40] and the suggestion that the baryon asymmetry is reflected in the dark matter sector [32]. While many previous WIMP searches—guided by the SUSY neutralino parameter space—paid much attention to ~100 GeV/c^2 WIMP masses, it is interesting in light of these new results to examine data with techniques optimized for much lower WIMP masses ~10 GeV/c^2. For this reason the timing-cut constructions considered so far were extended with lower thresholds (down to 5 keV for some detectors), in order to improve sensitivity to low-mass WIMPs.

All of the timing cuts presented so far were optimized for a 60 GeV/c^2 WIMP mass, and the corresponding analyses were restricted to a recoil-energy threshold of 10 keV. For events above this threshold the best estimates of surface-event background leakage are about one event. While the surface-event leakage is worse for the extended-threshold analyses, for low WIMP masses sensitivity improves considerably because of the steeply rising WIMP spectrum. Simple extensions to the three timing analyses were accomplished by lowering the thresholds, confirming the cut efficiencies below 10 keV, and reevaluating the surface-event leakage estimates. The analysis region for the extended analyses is approximately 5–15 keV (threshold differs by detector; see below), since recoils of light WIMPs ($\lesssim$10 GeV/c^2) with energies greater than 15 keV are very rare.

For the extended analyses there are several small changes to the event selections that help to maximize the sensitivity to WIMP masses below 10 GeV/c^2.

A careful study of the leakage induced by lowering the charge threshold showed that for light WIMPs with similar cross sections to the CDMS II silicon result [39] a net gain is obtained by lowering the charge threshold to 3.0 standard deviations above the mean noise value. We therefore modified the charge threshold to this value for the extended analyses. The recoil-energy threshold was then effectively set by the condition that signal events have an ionization yield below the mean -3σ ER band line. Of course, signal events were still required to be within the mean $\pm 2\sigma$ NR band (with the usual slight modification for the 5d-χ^2 analyses). Finally, the signal regions were taken to range from threshold up to 15 keV since this is the region that is expected to add significantly to the low-WIMP-mass exposure. These changes are implicit where we use the abbreviation "NRSS" in the context of the extended analyses. Most of the timing cuts (except the 5d-χ^2, see below) did not have their decision boundaries reoptimized for lower WIMP masses; the thresholds were simply extended and the changes above were made.

The 5d-χ^2 method, in addition to lowering the thresholds, was partially reoptimized for a 8 GeV/c^2 WIMP mass. The definitions of the χ^2 variables (χ^2_N,χ^2_B) remained the same. Additionally, the means and covariances were

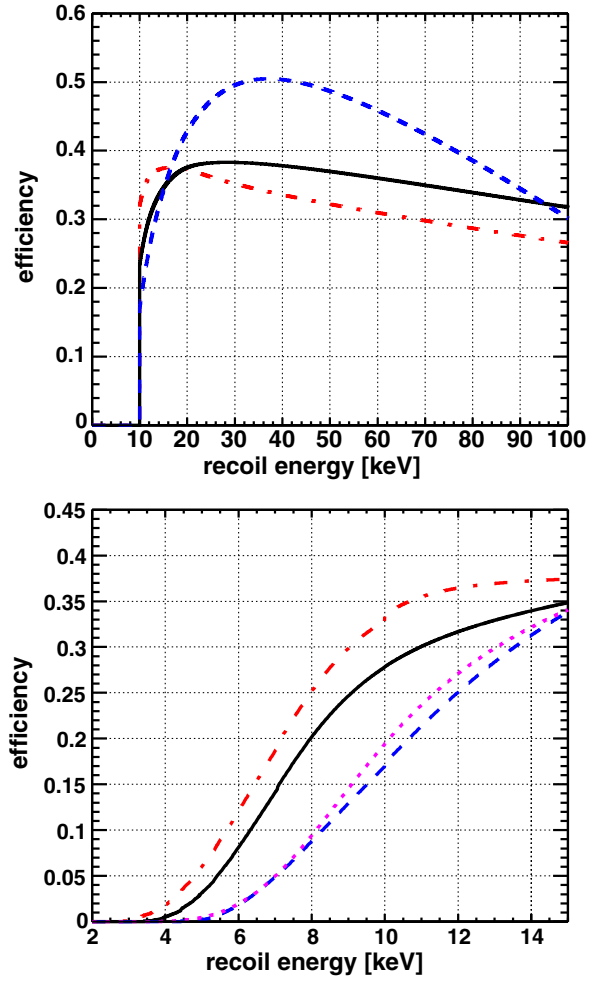

FIG. 10 (color online). Total combined efficiencies for all timing analyses. (Top panel) Efficiencies for the 10 keV threshold analyses. The SAEs (60 GeV/c^2 WIMP) are 219.1 kg days for the classic analysis (black solid), 216.4 kg days for the neural-network analysis (red dot-dashed), and 262.3 kg days for the 5d-χ^2 analysis (blue dashed). (Bottom panel) The efficiencies for the extended-threshold analyses with the addition of the 5d-χ^2 analysis optimized for a 8 GeV/c^2 WIMP mass (magenta dotted). All of the analyses have a total exposure (before efficiency reductions) of 612.2 kg days.

taken to have the same functional dependences given in Eqs. (5) and (6). The optimized yield cut was an asymmetric cut, with parameters $t = 1.8$ and $b = -1.9$, the same as the regular 5d-χ^2 analysis. The reoptimized sensitivity for the 8 GeV/c^2 was not significantly better than the standard 5d-χ^2 analysis, and not as good as the sensitivity for the classic extended-threshold analysis. Therefore, this reoptimization was not carried any further and the 60 GeV/c^2 optimized version is used.

E. Timing efficiencies and summary

Energy-dependent efficiencies for the timing analyses were computed using neutrons from the ^{252}Cf calibration data. Figure 10 presents the combined efficiencies of all cuts (quality, fiducial volume, yield, and timing) for each timing analysis. Above a 10 keV threshold, the 5d-χ^2 analysis has the best sensitivity and the highest SAE for a 60 GeV/c^2 WIMP (see Fig. 10 caption). The classic analysis has the second-best SAE, and provides continuity with the original analysis of this data set [33]. The neural-network analysis yields the smallest SAE, but has the best efficiency just above a 10 keV recoil energy threshold. For the extension of the analysis to below 10 keV, the classic timing analysis has the best sensitivity (though not the highest efficiency at low recoil energies; see Fig. 10). As mentioned in Sec. V, the 5d-χ^2 is our "primary" method above 10 keV and the classic is the primary extended-threshold method.

The efficiency function is a necessary ingredient for producing the limits and any uncertainty on this function is also present in the final limit. The trigger efficiency uncertainty is ~1% across the energy range; this is mostly statistical uncertainty. Our quality cut efficiency is calculated based on baseline noise levels using large event populations and so it has negligible uncertainty. Efficiencies of the other cuts are measured by selecting neutron populations in ^{252}Cf data and observing the decrease in the population by the application of the cuts in bins of recoil energy. The results are then fit with an empirical functional form with a low-energy falloff similar to the error function. Fiducial-volume, ionization-yield and phonon-timing cuts each contribute about a 5% statistical uncertainty. This measurement method is, however, prone to error due to the fact that neutrons can have multiple scatters inside a detector, while WIMPs cannot. In the case of the fiducial-volume cuts we used a Monte Carlo simulation to find a 5% discrepancy for multiple scatters, and corrected for it. Overall we assign a conservative 3% systematic uncertainty on the fiducial-volume and yield cuts for the effect of multiple scattering. Based on these estimates, using the averaged sizes of each efficiency, we expect the total uncertainty on the efficiencies to be ~6%. Generally this is negligible on the scale that our final limits are presented. A specific study of the efficiencies for the extended-threshold analysis below 6 keV showed that for the extended-threshold limits this total uncertainty becomes ~10% at the lowest WIMP mass (6.26 GeV/c^2) and drops to ~7% by a WIMP mass of 7 GeV/c^2.

TABLE II. Information about the three WIMP candidate events above 10 keV. Under "Analysis," "NN" refers to the neural-network timing analysis and "2010" refers to the original analysis of these data [33]. Note that no candidate events are observed for the 5d-χ^2 analysis.

Detector	Recoil energy [keV]	Yield	Analysis
T1Z5	12.30	0.33	NN, Classic, 2010
T2Z3	10.81	0.33	Classic
T3Z4	15.35	0.26	2010

VI. UNBLINDING

A blinding technique was used to avoid bias in the setting of data selection cuts. The current work used what can be referred to as "hidden signal box" analysis [68] which is common in rare-event searches where the signal region is known *a priori*. The same data were analyzed previously [33], but since all the data were reprocessed with an upgraded charge reconstruction algorithm, and the cuts were optimized solely based on calibration data and distributions outside the newly masked signal region, this is a good approximation of a hidden signal box analysis. Signal events were hidden by removing the single-scatter events in the NR yield band. This technique is effective for removing bias in the timing-cut preparation, but restricts the information that can be used for estimating surface-event leakage before unblinding has occurred. For this reason the leakage estimates were done before and after the unblinding, but consistency between the two methods is checked. Including the post-unblinding version using the NR singles that fail the timing cut made the final estimate more robust.

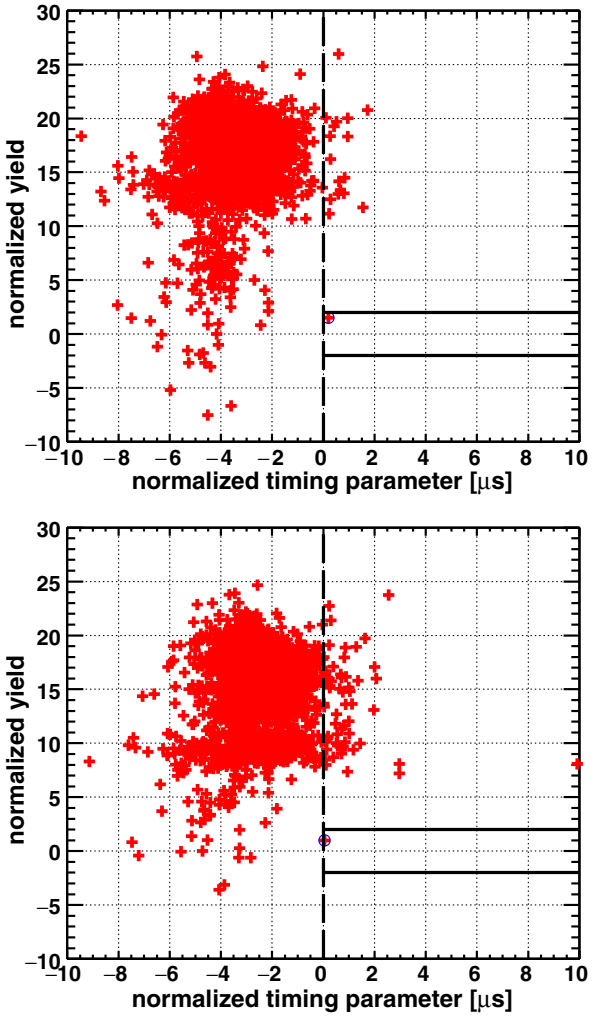

FIG. 11 (color online). Distributions of WIMP-search events in the detectors containing the two candidate events for the classic timing analysis: T1Z5 (top panel) and T2Z3 (bottom panel). The normalized yield is the distance from the average NR yield in units of the standard deviation of the yield distribution; the black horizontal lines on the right side of the plot indicate the $\pm 2\sigma$ NR band. The normalized timing parameter is the standard timing parameter ($t_{\mathrm{del}} + \tau$) minus the value of the cut boundary. WIMP-search events (red crosses) to the left of the timing cut (vertical black dashed line) pass all cuts except phonon timing and yield; events to the right of that line pass the timing cut, and those that are also in the NR band (solid black lines) pass the yield cut. The highlighted event (blue open circle surrounding red cross) in the top panel is candidate 1 and the highlighted event in the bottom panel is candidate 2 (see Table II). All the events shown are in the recoil energy range 10–100 keV.

Upon unblinding, the following number of events pass all cuts above 10 keV: zero for the 5d-χ^2 timing analysis, two for the classic timing analysis, and one for the neural-network analysis. One of the two candidates from the original analysis is a candidate in both the classic timing and the neural-network analyses [33]. The second candidate from that analysis, whose poor charge-pulse fitting prompted this reanalysis (see Sec. III), failed all timing analyses by a substantial margin. Information about the two passing candidate events is shown in Table II. Figure 11 shows the location of these events within the signal region of the classic analysis.

Our extended-threshold analyses gave a wide range in terms of the number of candidate events. The classic analysis had six candidates and the neural-network analysis had 16. No events were observed in the extended version of the 5d-χ^2 analysis. A description of the candidate events for our primary extended-threshold analysis (the "classic" cut) is given in Table III. The large number of candidate events in the neural-network analysis is attributed to an increased leakage of anomalously low-ionization events, those that are normally below the ionization threshold in the 10 keV analysis [62]. This increased leakage of essentially zero-ionization events was not expected and is presumably due to a bias in the training set of the neural network. It has negligible contribution above the original 4.5 standard deviation charge threshold. The low number of events in the 5d-χ^2 analysis is not unexpected because that cut has an independent energy bin at 10–20 keV, where the cut is rather stringent because of increasing leakage at low energy and the optimization to exposure at a 60 GeV/c^2 WIMP mass.

TABLE III. Information about the six WIMP candidate events for the "classic" extended-threshold analysis.

Detector	Recoil energies [keV]
T1Z5	3.45, 5.73, 12.30
T2Z3	10.81
T4Z4	7.56
T4Z5	7.25

TABLE IV. Expected leakage and exposure statistics for all of the surface-event rejection methods described in this work. For the extended-threshold analyses, we quote 5 keV as an approximate lower limit on the signal region. The actual threshold depends on the detector and is set by the crossing of the ER band limits and the charge threshold curves (see Sec. V D). The symbol $>$ is used to indicate lower limits on the expected leakage. In those situations the event sets that are typically used to estimate the leakage do not have events all the way down to the signal-region threshold (see text).

Method	Energy range [keV]	Exp. leakage	Candidates	WIMP mass [GeV/c^2]	SAE [kg days]
Classic	10–100	$0.64^{+0.17}_{-0.15}$	2	60	220
Neural Network	10–100	$0.87^{+0.24}_{-0.21}$	1	60	216
5d-χ^2	10–100	$1.19^{+0.23}_{-0.21}$	0	60	250
Classic ext.	5–15	$>1.48^{+0.20}_{-0.20}$	6	60	186
Neural Network ext.	5–15	$>1.39^{+0.21}_{-0.21}$	16	60	190
extended 5d-χ^2	5–15	$>0.97^{+0.15}_{-0.15}$	0	60	202
extended 5d-χ^2	5–15	$>1.82^{+0.31}_{-0.31}$	0	8	3.78[a]

[a]SAE depends on an assumed WIMP mass [see Eq. (4)]; we use the optimization mass in all cases. For this reason SAE is only comparable in situations of common optimization mass and signal-region energy range.

The post-unblinding leakage estimates can be found in Table IV along with the analysis energy ranges, candidate numbers, exposures and WIMP-mass optimization assumptions.

VII. ESTIMATED BACKGROUNDS

A. Surface electron-recoil background

Surface electron recoils originate from several sources: 1) particles emitted from β emitters contaminating the surfaces of the detector and the material around it (notably ^{210}Pb), 2) photo-electrons emitted from material neighboring the detector through Compton scattering or the photoelectric effect, and 3) photons that interact in the detector within a few microns of the surface. Photons from category 3) can be low-energy x rays or high-energy photons that Compton scatter in the detector. Past studies showed that the dominant contributions are from ^{210}Pb and photon-induced backgrounds, which contribute approximately equally. No other sources were found to be statistically significant.

The expected number of surface events leaking into the WIMP signal region was calculated using the number of single scatters in the NR band that are rejected by the timing cut and the surface-event rejection efficiency. The surface-event rejection efficiency was estimated from three independent event sets and combined to improve accuracy. To reduce systematic uncertainties, leakage estimates were calculated on a detector-by-detector basis (index i below) and where possible the relevant event set was separated into bins (index j below) of energy and approximate event position (see "face" bins below). In every case the leakage can be expressed as

$$n = \sum_{i,j} N_i s_{ij} \frac{m_{ij}}{M_{ij}}, \tag{10}$$

where n is the total expected number of surface events leaking into the WIMP signal region. The symbol N_i is the number of NRSS events in the NR band rejected by the timing cut for the ith detector. M_{ij} and m_{ij} are the number of multiples in (or around; see below) the WIMP signal region failing and passing the timing cut, respectively. The s_{ij} are the fractions of N_i in subset j, which are calculated using the surface-event multiples in the NR band for the WIMP-search data.

The 14 detectors used in this analysis were split into two detector sets according to their positions in the tower: the 12 interior detectors, and two "end caps," on the top or bottom of a stack of six detectors. Equation (10) was applied to each detector set separately because end caps require additional systematic uncertainty corrections (discussed below). The M_{ij} and m_{ij} are determined independently for three different event sets: 1) NRMS in WIMP-search data, 2) WBMS in WIMP-search data, and 3) WBMS in ^{133}Ba calibration data. For representative surface-event populations drawn from outside the NR band, the index j specifies one of six subsets constructed from two detector faces (see Sec. IV B on face tagging) and three energy bins (10–20 keV, 20–30 keV, and 30–100 keV). In the case where M_{ij} and m_{ij} were drawn from the NRMS WIMP-search data, the six event subsets were combined for each detector because of the low statistics, reducing the index set for j to one element. Each of the three independent estimations of m_{ij} and M_{ij} are used with Eq. (10) to obtain three estimators for n, which were then statistically combined to produce the final leakage estimate.

With these estimators, Monte Carlo (MC) simulations and Bayesian inference were used to estimate the surface-event background and its uncertainties after unblinding the data [66]. Instead of simulating the posterior distribution of n [Eq. (10)], for each event set, MC simulations are run for the posteriors of the individual Poisson counts m_{ij} and M_{ij},

and the multinomial fractions s_{ij}. Jaynes priors, $p(\rho) \propto \rho^c$ with $c \approx -1$, were chosen for the Poisson distribution. This prior is generally considered an "objective prior," having the advantage of ensuring invariance of statistical inference under transformations of the Poisson mean [69]. A uniform prior was used for the multinomial distribution. The posterior of n was then calculated using Eq. (10) with the simulated posteriors of each component.

Systematic uncertainties of different origins were estimated independently, added in quadrature, and then incorporated into the posterior of the leakage with a profile of the standard normal distribution. Systematic uncertainties from two sources were estimated, for all the detector and data-set combinations, including the choice of the prior exponent c and the difference between singles and multiples.

End-cap detectors can have their multiples tagged only on one side. This biases the counts of singles upward in these detectors. Together with the low number of surface events in the data, it is challenging to estimate the surface-event background. As a result, a conservative estimate where we allow the s_{ij} to be biased higher for end caps—the detectors with the worst leakage—is used. As a double check, the component leakages for each detector obtained by the Bayesian approach were compared to those obtained by the frequentist approach [70]. There is good agreement between the two.

The final surface-event leakage estimates incorporating both systematic and statistical uncertainties are displayed in Table IV for all timing cuts presented in this work. The analyses with the best expected sensitivities give leakage estimates of $1.19(+0.23-0.20)$ events (5d-χ^2 for the 10 keV threshold analysis) and $>1.48(+0.20-0.20)$ events (classic extended threshold). The leakage estimate for the extended-threshold analysis is a lower limit because our standard background sample does not extend all the way down to the signal-region threshold. WIMP-search multiple scatters below the ER mean -5σ line and above the NR mean +2σ line (WBMS) is one of our typical background samples, but because the ER mean -5σ and NR band lines cross there is an implicit energy threshold in this background sample. The signal region, however, is taken to be the NR band above the 3σ charge threshold and below the ER mean -3σ line. This leaves a small region (see Fig. 5) that is unaccounted for in the background estimates. The estimate is nevertheless useful because 1) the implicit background-estimation threshold can be as low as ~5 keV, very near the signal-region threshold in most cases, and 2) the limits are calculated without background subtraction so a conspicuous rise in the WIMP upper limit would exist if there were a large leakage present in the unaccounted region.

B. Cosmogenic background estimate

To estimate the cosmogenic neutron background, a combination of simulation and data was used [71]. Parent muons that intersect the CDMS II 5-cm-thick scintillator panels are vetoed at nearly 100% efficiency. Our data contains only a small number of neutrons that accompany identified muons, so a high-statistics simulation was used to estimate how many veto-coincident neutrons produce NRs in the Ge ZIP detectors, compared with those that are not accompanied by veto activity.

Simulation muons generated using the MUSUN [72] program based on slant-path data from Soudan2 angular muon flux measurements [73] were used as input to a GEANT4 MC model of the Soudan CDMS II experimental setup. These muons have a mean energy of ~215 GeV and azimuthal and zenith distributions characteristic of the overburden of the Soudan site and depth (2090 m.w.e.). The simulated muons were generated with the appropriate angular distributions and spectra on a five-sided parallelepiped (no floor). They were then propagated via GEANT4 through 10 m of rock into the Soudan hall. All secondaries and the parent muon(s) were tracked through a complete geometry of the CDMS II shielding and detector towers. In the simulations, the CDMS setup is located asymmetrically 2 m from one wall of the 8 m east-west cavern dimension to reproduce albedo effects. The statistics correspond to 66 live years. A multiple is defined in the simulation output as an NR in a Ge detector accompanied by energy deposition of any sort above 2 keV in any other ZIP detector.

In an effort to balance the statistical and systematic uncertainties, three complementary estimators for the total number of unvetoed single-scatter events were constructed. For the first two estimators, the simulation was used to calculate a veto ratio (unvetoed to veto-coincident NRs) that was then normalized to the veto-coincident data from the WIMP-search measurements to establish the background estimate. The second estimator makes use of the higher-statistics multiple-scatter sample, whereas the first uses only single scatters. The third estimator uses only simulated unvetoed single-scatter events, scaled to the correct experimental live time, and accounts for the detector efficiencies for each timing analysis.

The veto ratio is 0.008 ± 0.003 for single scatters and 0.003 ± 0.001 for multiple-scatter NR events in the simulation. One might expect a smaller veto ratio for multiple-scatter events if they are taken to represent more pervasive showers; excess energy from those showers will often be detected by the veto system even when the parent muon misses the scintillator panels. The weighted average for all events gives a veto ratio of 0.004 ± 0.001.

There are 14 Ge NR events in our veto-coincident data, of which three are single scatters. This is in agreement with the MC which predicts that ~26% of the vetoed events should be singles, and the rest multiples. Of the vetoed NR events, five pass the 5d-χ^2 timing cut and four pass the classic or neural-network timing cuts. For the data-driven estimators, we normalize to those passing the timing cut, rather than introduce additional systematic uncertainty by

applying an average timing-cut efficiency to all 14 detectors in the simulation. However, the numbers obtained either way are consistent, with trade-offs between systematic uncertainty and statistical uncertainty in each case. We decided to quote the simulation-driven estimate because it is consistent with the others and offers the best statistical uncertainty. The systematic uncertainty is taken as the spread between all the estimators.

Based on the 16 unvetoed NR singles over 66 live years of simulation data, the 5d-χ^2 timing-cut cosmogenic neutron background is $0.021 \pm 0.008_{\text{stat}} \pm 0.009_{\text{sys}}$ events for the 10 keV analysis. The classic and neural-network cuts give $0.019 \pm 0.007_{\text{stat}} \pm 0.01_{\text{sys}}$ events and $0.018 \pm 0.007_{\text{stat}} \pm 0.01_{\text{sys}}$ events respectively for the 10 keV threshold case.

The estimates were also made for the extended-threshold analyses by using the energy range 2–20 keV to approximate the extended-threshold energy ranges. Based on 12 unvetoed NR singles in that range over 66 live years the 5d-χ^2 extended timing-cut cosmogenic neutron background is $0.009 \pm 0.004_{\text{stat}} \pm 0.001_{\text{sys}}$ events, the classic is $0.012 \pm 0.005_{\text{stat}} \pm 0.004_{\text{sys}}$ events, and the neural network is $0.014 \pm 0.006_{\text{stat}} \pm 0.009_{\text{sys}}$ events.

C. Radiogenic background estimate

The radiogenic neutron background was also estimated using a GEANT4 simulation of the CDMS II tower configuration. Neutrons originating from the Th and U decay chains were simulated for each material in the setup (lead, polyethylene, copper). The primary energy spectra of the neutrons was generated using the SOURCES4C package [74–76], which computes the neutron spectra due to spontaneous fission and (α, n) reactions of alphas from the full decay chains within the matrix material. The neutrons were propagated through all materials, eventually creating NRs in the Ge and Si detectors. The single- and multiple-scatter rates were tabulated for each detector to create high-statistics files labeled by their contaminant source. The files were then weighted by the contamination level (see below) and normalized to the amount of material present to determine the final background rate. The source with the highest single-scatter contribution is ^{238}U in the copper cryostat enclosures (cans), followed closely by U and Th contaminants in the lead shielding.

The contamination levels were determined by a separate γ simulation, again using GEANT4 and the same CDMS II geometry. In this simulation, gammas from the ^{232}Th and ^{238}U decay chains, ^{40}K, and ^{60}Co were generated from inside the shielding components and tower structures, and from radon daughters on surfaces. In order to reproduce the fiducial-volume cut already applied to the data, the location of the energy deposition and the electric field map in the detectors were used to deduce the fraction of charge collected on the inner and outer electrodes. The event was cut if it produced a measurable signal on the outer electrode. A charge threshold was implemented in the simulation data by using the experimental inner-electrode charge thresholds (in keV$_{\text{ee}}$) and applying them to the inner-electrode energy derived from the above procedure.

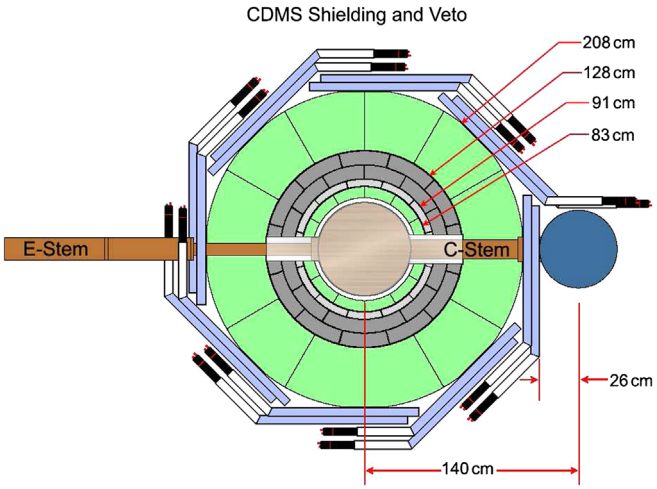

FIG. 12 (color online). Schematic of the CDMS II shielding configuration. The outermost vacuum can surface is shown near the center and radially outward the layers are inner polyethylene (green), inner lead (light grey), outer lead (darker grey), outer polyethylene (green), and muon-veto scintillator counters (blue) with attached light guides and phototubes (white and black). Cooling of the detectors is achieved through the "cold stem" from a dilution refrigerator (dark blue), while cabling passes through the "electronics stem" on the other side of the setup.

To obtain the contamination estimate a χ^2 minimization was performed to fit the 43 sources considered (see Fig. 12 for a schematic of the setup and Table V for a breakdown of source locations) to the ER data above 15 keV$_{\text{ee}}$, avoiding the $\sim$10 keV$_{\text{ee}}$ Ge activation peaks. Some representative values for this contamination are 4 mBq/kg for both ^{232}Th and ^{238}U in the inner polyethylene shield and $6-7$ mBq/kg for ^{232}Th and ^{238}U in the tower 5 copper, the tower with the highest contamination. The comparison between the ER spectrum and the sum of MC results using the best-fit contamination levels is shown in Fig. 13.

Because of nearly degenerate fits to the spectrum, there is uncertainty in the final contamination values. The degree of uncertainty was estimated by bracketing the largest changes that produce acceptable fits in the gamma MC and translating these into the resulting changes in the neutron rate.

In the 14 Ge detectors used for the WIMP-search analysis, the expected raw radiogenic neutron single-scatter background rate was found to be $(1.15 \pm 0.14) \times 10^{-4}$ events/kg/day in the 10–100 keV energy range. The statistical uncertainty is negligible because of the large number of events simulated while the systematic uncertainty listed is due to the uncertainty in the contamination values and locations. This singles spectrum was then convolved with the final neutron cut efficiencies from the three timing analyses (see Fig. 10). The radiogenic

TABLE V. Sources used for the radioactive contamination fitting procedure. The ✓ indicates that the respective source was used in the fitting procedure for the location given. The cans are the nested copper cold stages of the cryostat, where surface sources were simulated on both the innermost and outermost surfaces. There are five separate sources for the copper components of the five detector towers. No simulated sources were placed in the outer polyethylene or the veto panels because they are behind too much shielding to yield a measurable amount of background.

Contamination	Outer lead	Inner lead	Inner polyethylene	Cans	Innermost can surface	Outermost can surface	Towers
^{60}Co	✓	…	…	✓	✓	✓	✓
^{40}K	✓	✓	✓	✓	✓	✓	✓
^{232}Th	✓	✓	✓	✓	✓	✓	✓
^{238}U	✓	✓	✓	✓	✓	✓	✓
^{222}Rn	…	…	…	…	…	✓	…

spectrum-averaged efficiencies are 35.3% for the classic, 34.9% for the neural net, and 40.4% for the 5d-χ^2 analysis. For the raw exposure of 612.2 kg days, the final radiogenic neutron event backgrounds for the three analyses are $0.025 \pm 0.0001_{\text{stat}} \pm 0.003_{\text{sys}}$ events for the classic and neural network, and $0.028 \pm 0.0001_{\text{stat}} \pm 0.004_{\text{sys}}$ events for the 5d-χ^2 analysis.

For the extended analyses the estimates were made with the approximate energy range 2–20 keV. The estimates were $0.0131 \pm 0.0001_{\text{stat}} \pm 0.0019_{\text{sys}}$ for the classic, $0.0148 \pm 0.0001_{\text{stat}} \pm 0.0021_{\text{sys}}$ for the neural network, and $0.0105 \pm 0.0001_{\text{stat}} \pm 0.0015_{\text{sys}}$ for the 5d-χ^2.

D. ^{206}Pb background estimate

^{210}Po decays via the α-decay process. This leaves an α particle of 5.4 MeV and a recoiling ($\lesssim$100 keV) ^{206}Pb nucleus in the final state. ^{210}Po is in the ^{238}U decay chain and is part of possible post-^{222}Rn plate-out contamination. It is also the first post-^{222}Rn α-decayer after the long-lived ^{210}Pb. These facts make this decay likely to be an important long-lived contamination, and because a recoiling ^{206}Pb nucleus could have produced an energy deposition below ~100 keV with an ionization yield consistent with being an NR, it makes sense to evaluate this background very seriously.

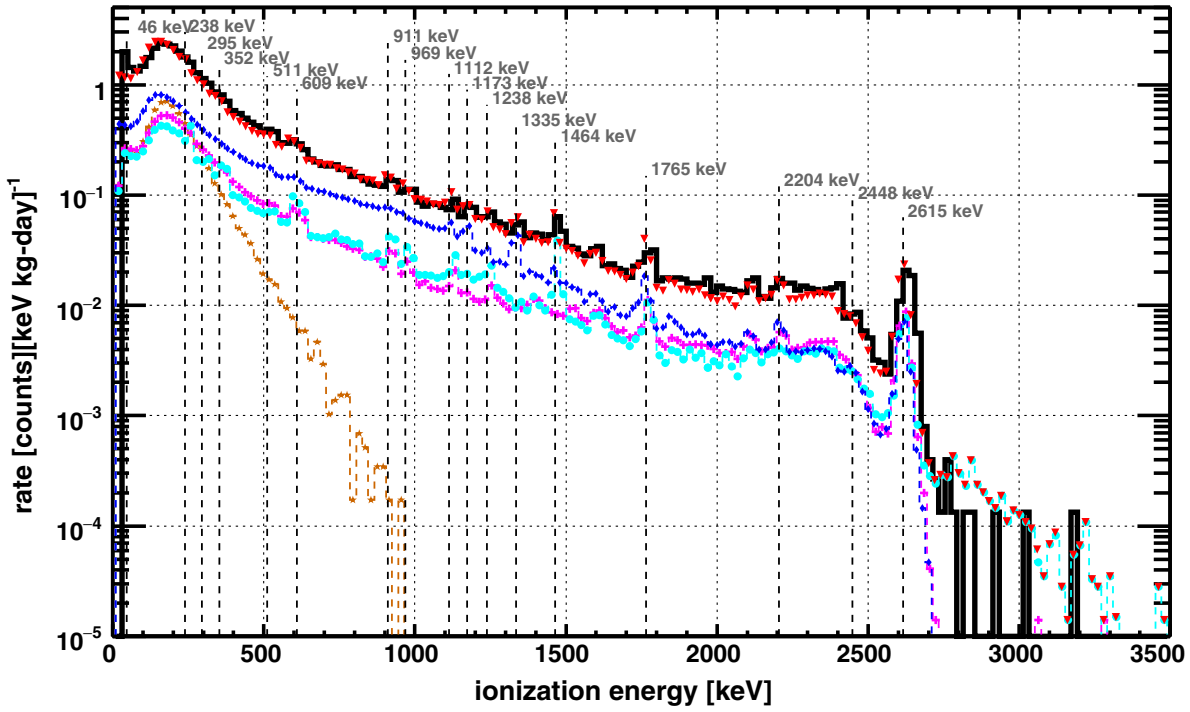

FIG. 13 (color online). Measured event-summed energy across all detectors (black solid line) compared to simulations of contaminants from common locations: lead shielding (blue diamonds), inner polyethylene shielding (magenta crosses), copper cans and tower components (cyan filled circles), and outermost can surfaces (brown stars). The sum of all simulated components (red inverted triangles) is also plotted and is in good agreement with the measured data.

Because of the CDMS II detector geometry (see Fig. 1) much of the surrounding surface of an interior detector is comprised of another detector. ^{210}Po decay events in which the decay occurs in one detector and the ^{206}Pb recoil is registered in an adjacent detector cannot contaminate the signal region of the latter detector because of the clear 5.4 MeV α deposition in the former. Therefore the most important component of the background comes from surfaces that are uninstrumented or those that are adjacent to uninstrumented surfaces. Another important point is that since the alphas from this decay give such a clear signature, and the decay is a two-body decay, an obvious way to estimate the number of unaccompanied (single) ^{206}Pb events is to estimate the number of unaccompanied α events from the decay. The angular distribution is isotropic and any surface that can observe a single α is approximately equally likely to observe a single ^{206}Pb recoil. This estimation of the number of single ^{206}Pb events was carried out, and using rough estimations for the passage fractions of these events when subjected to the other analysis cuts, we expect approximately 0.187 signal-region ^{206}Pb events over the whole exposure.

Since the ^{206}Pb recoil estimates were inferred from α counting, and the ^{206}Pb recoils can come at different energies depending on how deeply the ^{210}Po parent is embedded into the originating surface, we do not have a good specification of the energy distribution of such events. Therefore, to be conservative we can use the same estimate for the 10 keV and extended-threshold analyses. We expect $0.187 \pm 0.018_{\mathrm{stat}} \pm 0.187_{\mathrm{sys}}$ events over the whole exposure; and have assigned a 100% systematic uncertainty to account for the roughness of this estimate. This background estimate is clearly subdominant with respect to the surface-event background estimates, but is larger than the cosmogenic or radiogenic neutron background estimates [62].

VIII. RESULTS

The background estimates for the primary 10 keV and extended-threshold analyses are summarized in Table VI. While the background estimates can be used to interpret the overall results of the experiments they do not directly modify the limit curves (see below).

TABLE VI. A summary of the background estimates from the primary analysis methods. Statistical and systematic uncertainties have been added in quadrature and to compute the total backgrounds all component uncertainties were also added in quadrature.

Background	5d-χ^2 (10 keV)	Classic (extended)
Leakage	1.19 ± 0.22	$>1.48 \pm 0.20$
Cosmogenic	0.021 ± 0.012	0.012 ± 0.006
Radiogenic	0.028 ± 0.004	0.013 ± 0.002
^{206}Pb	0.19 ± 0.19	0.19 ± 0.19
Total	1.43 ± 0.30	$>1.69 \pm 0.28$

Results of direct WIMP-search experiments are usually summarized as upper limits or signal contours in the WIMP-nucleon cross section versus WIMP-mass plane. Yellin's optimum interval method [77] allows derivation of an upper limit on a signal rate in cases with unknown background. While the backgrounds in our signal region are not completely unknown, this is a conservative approach to setting upper limits on a possible signal. This presentation also requires assumptions about the WIMP distribution in the galactic halo, the type of interaction between WIMPs and nucleons, and the nuclear form factor for the interaction. The velocity distribution was assumed to be Maxwellian and was parametrized by the rotational velocity at infinite radius and corrected for the finite galactic escape velocity [49], which is taken to be 544 km/s [78]. A WIMP mass density of 0.3 GeV$/c^2/$cm^3 was used for historical reasons, making the computed limits comparable to similar publications [49]. Some recent astrophysical measurements indicate different values [79]; a correction for such deviations is a simple multiplicative factor and can be easily applied by the reader [80]. A most probable WIMP velocity of 220 km/s was used along with a mean circular velocity of the Earth with respect to the Galactic center of 232 km/s. The WIMP interactions were assumed to be spin independent and the Helm form factor was used [49] for a natural Ge isotopic distribution.

The comparison of the present 10 keV 5d-χ^2 and classic extended results with other published limits and signal contours is shown in Fig. 14. In the figure, our 10 keV 5d-χ^2 limit is combined with the CDMS II five-tower exposure acquired before July 2007, resulting in a limit that summarizes the full (and final) CDMS II high-threshold sensitivity. The CDMS II/EDELWEISS combined limit [35] is also shown for comparison. Above $\sim$100 GeV$/c^2$ WIMP mass the combined limit is comparable to our CDMS II combined result owing to the good efficiency-averaged exposures of both of the experiments in the relevant energy ranges.

A. Limit cross-checks

To gain insight into the effect of timing-cut figures of merit (efficiency, SAE, leakage) on WIMP-search results, we have constructed final limits for all of the timing-cut constructions in this work. Although the SAE and expected leakage were exclusively used to choose the primary timing cuts, comparing all of the limits in this way gives cross-checks on how other parameters (efficiency, signal-region events) affect the reach of the experiment.

The top part of Fig. 15 shows the limits derived using the optimum interval method for the different timing cuts with 10 keV thresholds. Relative to the original publication, the ionization-based fiducial-volume and phonon-timing cuts have improved efficiencies in the analysis reported here,

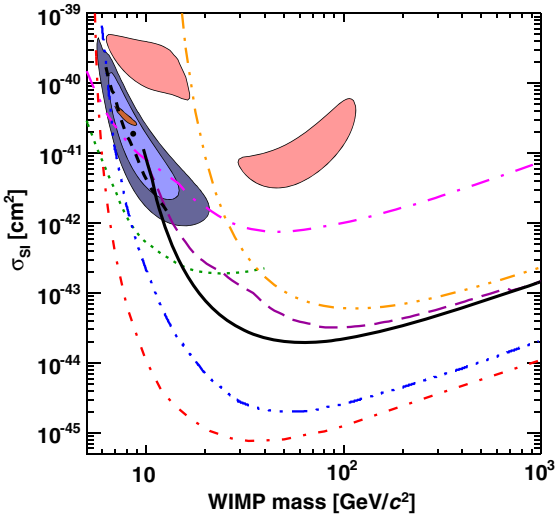

FIG. 14 (color online). This figure compares the main results from this analysis (the current 5d-χ^2 analysis combined with prior CDMS II exposures, black solid and the classic extended-threshold analysis, black dashed) with previously published results (all limits are at 90% C.L.): Darkside-50 [81] (orange triple-dot-dashed); XENON100 [82] (blue triple-dot-dashed); LUX [83] (red dot-dashed); SuperCDMS low-threshold [84] (green dotted); CDMS II/EDELWEISS combined [35] (purple long dashed); CRESST-II [85] (magenta long-dot-dashed); CDMS II Si [39] (90% and 68% C.L. contours, blue, with the best-fit point marked with a black dot); DAMA/LIBRA [43,86] (3σ region, light red) and CoGeNT [40] (90% C.L., brown).

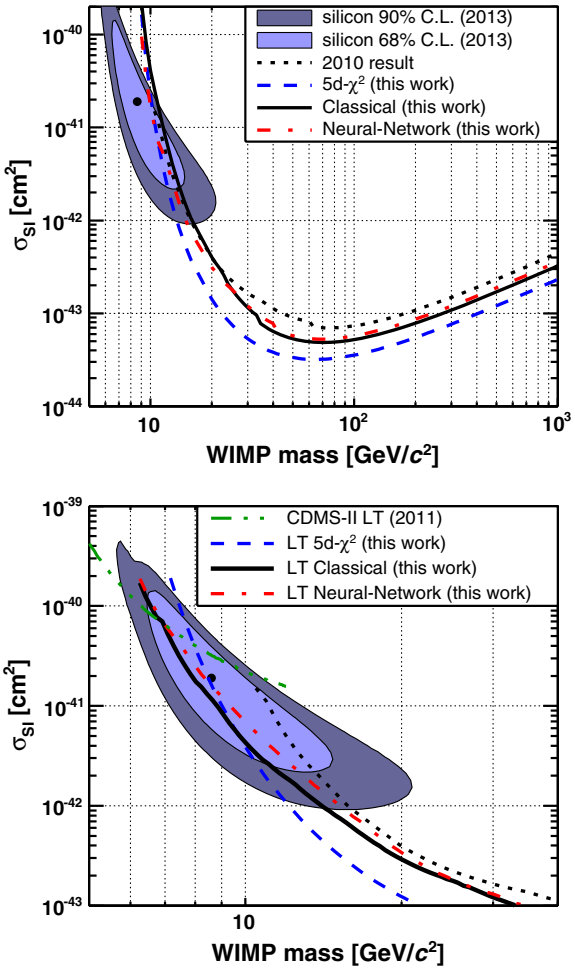

FIG. 15 (color online). Experimental upper limits (90% confidence level) derived from each of the analyses presented in this work compared with the originally published [33] (black dotted) limits. The CDMS II Si contour is shown with the best-fit point marked with a black dot (WIMP mass of 8.6 GeV/c^2 and WIMP-nucleon cross section of 1.9×10^{-41} cm^2) [39]. (Top panel) The 10 keV threshold analyses. The 5d-χ^2 limit (blue dashed) is the "primary" high-threshold result to be quoted from this work. The neural-network and classic limits are shown as red dot-dashed and black solid lines respectively. (Bottom panel) The extended-threshold limits, focused on the lower WIMP-mass region. The same color code applies except that all of the analyses from this work correspond to the extended-threshold versions. The classic limit (black solid) is the "primary" extended-threshold result to be quoted from this work. The extended 5d-χ^2 limit shown corresponds to the timing-cut optimization assuming a 60 GeV/c^2 WIMP mass. For comparison, the previous CDMS II low-threshold limit is shown [34] (green triple-dot-dashed).

leading to the improved exposure and more stringent limits. In terms of the overall spectrum-averaged detection efficiency for a 60 GeV/c^2 WIMP, the classic timing-cut strategy (see Sec. V A) shows a 12% improvement over the previously published version, about half of which can be attributed to a reoptimization of the ionization-based fiducial volume following the data reprocessing. A similar improvement was seen for the neural-network timing-cut analysis (described in Sec. V B). The largest improvement of 29% in overall SAE efficiency was achieved for the 5d-χ^2 analysis (described in Sec. V C), owing primarily to an increased timing-cut efficiency in the 15–90 keV energy range (see Sec. V E).

For the 10 keV-threshold analyses, the 5d-χ^2 sets the most stringent limit at a 60 GeV/c^2 WIMP mass, while the neural-network timing cut results in stronger limits at and below 10 GeV/c^2, an important region for further study [39]. The 5d-χ^2 set weaker limits for low-mass WIMPs because the cut was set to maximize sensitivity to a WIMP with mass 60 GeV/c^2. This combined with the fact that the 5d-χ^2 method could set a very tight cut at low energies (it used an independent 10–20 keV bin whereas the other analyses were less granular) produced a poorer WIMP efficiency toward low recoil energies despite the lower expected background leakage at those energies, but excellent sensitivity for high WIMP masses.

The lower part of Fig. 15 shows the extended limits in the low-WIMP-mass region. Each extended analysis constrains the $8-10$ GeV/c^2 mass region more strongly than the higher-threshold analyses, and the classic timing cut produces the strongest limit near the silicon-detector analysis best-fit point of $M_W = 8.6$ GeV/c^2 and $\sigma_{SI} = 1.9 \times 10^{-41}$ cm^2 [39]. The extended limits are also compared to

the previous low-threshold CDMS II results, which did not use a timing cut [34]. That analysis has a larger exposure toward lower recoil energies which accounts for the stronger limit set below a $\sim 7\ \mathrm{GeV}/c^2$ WIMP mass. The classic analysis presented here has a stronger limit by a factor of approximately 2.7 at a WIMP mass of $\sim 8.6\ \mathrm{GeV}/c^2$.

IX. CONCLUSION

The reprocessed data did not produce significant changes in the number of signal-region events, indicating that uncertainties applied in the original processing of the CDMS II data set [33] were robust. All three sets of higher-threshold timing cuts produced similar limits, with small differences consistent with their corresponding exposure-optimization procedures. For example, the 5d-χ^2 analysis has a high efficiency at moderate recoil energies (30–60 keV), but has a stringent timing cut at lower energies. It is well suited to provide the strongest limits at high WIMP mass ($> 60\ \mathrm{GeV}/c^2$), but will produce fewer low-energy signal-region events. On the other hand, the classic analysis at the 10 keV threshold shows a slight weakening of the 90% C.L. limit for WIMP masses below about $18\ \mathrm{GeV}/c^2$, where sharp increases in the limit curves indicate systematics near threshold. The neural-network timing cut has been identified as a robust method with the highest signal efficiency at low energies (see Fig. 10) and good sensitivity at lower WIMP mass ($\leq 9\ \mathrm{GeV}/c^2$). The classic extended-threshold limit rules out about half of the silicon 68% C.L. region obtained in a previous CDMS II publication [39]. This indicates that the low-threshold results from the Ge detectors are marginally compatible with the Si-detector measurements taken during the same data period, under standard assumptions. Comparisons of such direct-detection results on different nuclei will be a powerful tool for understanding WIMP dark matter both in terms of the fundamental WIMP interactions [87,88] and possible backgrounds.

ACKNOWLEDGMENTS

The CDMS Collaboration gratefully acknowledges the contributions of numerous engineers and technicians; we would like to especially thank Dennis Seitz, Jim Beaty, Bruce Hines, Larry Novak, Richard Schmitt and Astrid Tomada. In addition, we gratefully acknowledge assistance from the staff of the Soudan Underground Laboratory and the Minnesota Department of Natural Resources. This work is supported in part by the National Science Foundation, the U.S. Department of Energy, NSERC Canada, and by MultiDark (Spanish MINECO). Fermilab is operated by the Fermi Research Alliance, LLC under Contract No. De-AC02-07CH11359. SLAC is operated under Contract No. DE-AC02-76SF00515 with the United States Department of Energy.

[1] F. Zwicky, Helv. Phys. Acta **6**, 110 (1933); Gen. Relativ. Gravit. **41**, 207 (2009).
[2] H. W. Babcock, Lick Obs. Bull. **498**, 41 (1948).
[3] Y. Sofue and V. Rubin, Annu. Rev. Astron. Astrophys. **39**, 137 (2001).
[4] K. G. Begeman *et al.*, Mon. Not. R. Astron Soc. **249**, 523 (1991).
[5] T. S. V. Albada, R. Sancisi, M. Petrou, and R. J. Tayler, Phil. Trans. R. Soc. A **320**, 447 (1986).
[6] B. J. Maughan, L. R. Jones, H. Ebeling, and C. Scharf, Mon. Not. R. Astron. Soc. **351**, 1193 (2004).
[7] A. D. Lewis, D. A. Buote, and J. T. Stocke, Astrophys. J. **586**, 135 (2003).
[8] J.-P. Kneib, R. S. Ellis, I. Smail, W. J. Couch, and R. M. Sharples, Astrophys. J. **471**, 643 (1996).
[9] J. P. Kneib *et al.*, Astron. Astrophys. **303**, 27 (1995).
[10] E. S. Sheldon *et al.*, Astrophys. J. **703**, 2217 (2009).
[11] E. S. Sheldon *et al.*, Astrophys. J. **703**, 2232 (2009).
[12] D. E. Johnston *et al.*, arXiv:0709.1159.
[13] J. D. Bekenstein, Phys. Rev. D **70**, 083509 (2004).
[14] M. Milgrom, Astrophys. J. **270**, 365 (1983).
[15] F. Kahlhoefer, K. Schmidt-Hoberg, M. T. Frandsen, and S. Sarkar, Mon. Not. R. Astron. Soc. **437**, 2865 (2014).
[16] D. Clowe, M. Bradač, A. H. Gonzalez, M. Markevitch, S. W. Randall, C. Jones, and D. Zaritsky, Astrophys. J. **648**, L109 (2006).
[17] G. W. Angus, H. Y. Shan, H. S. Zhao, and B. Famaey, Astrophys. J. **654**, L13 (2007).
[18] G. W. Angus, B. Famaey, and H. S. Zhao, Mon. Not. R. Astron. Soc. **371**, 138 (2006).
[19] M. Zemp, Mod. Phys. Lett. A **24**, 2291 (2009).
[20] J. Diemand and B. Moore, Adv. Sci. Lett. **4**, 297 (2011).
[21] M. Boylan-Kolchin, V. Springel, S. D. M. White, A. Jenkins, and G. Lemson, Mon. Not. R. Astron. Soc. **398**, 1150 (2009).
[22] A. G. Riess *et al.*, Astrophys. J. **607**, 665 (2004).
[23] S. Perlmutter *et al.*, Astrophys. J. **517**, 565 (1999).
[24] A. G. Riess *et al.*, Astron. J. **116**, 1009 (1998).
[25] R. H. Cyburt, B. D Fields, and K. A Olive, J. Cosmol. Astropart. Phys. 11 (2008) 012.
[26] D. J. Eisenstein *et al.*, Astrophys. J. **633**, 560 (2005).
[27] P. Ade *et al.* (Planck Collaboration), Astron. Astrophys. **571**, A1 (2014).
[28] G. Hinshaw *et al.*, Astrophys. J. Suppl. Ser. **208**, 19 (2013).
[29] M. Kowalski *et al.*, Astrophys. J. **686**, 749 (2008).
[30] B. W. Lee and S. Weinberg, Phys. Rev. Lett. **39**, 165 (1977).

[31] I. Aitchison, *Supersymmetry in Particle Physics: An Elementary Introduction* (Cambridge University Press, Cambridge, England, 2007).
[32] D. E. Kaplan, M. A. Luty, and K. M. Zurek, Phys. Rev. D **79**, 115016 (2009).
[33] Z. Ahmed *et al.* (CDMS Collaboration), Science **327**, 1619 (2010).
[34] Z. Ahmed *et al.* (CDMS Collaboration), Phys. Rev. Lett. **106**, 131302 (2011).
[35] Z. Ahmed *et al.*, Phys. Rev. D **84**, 011102 (2011).
[36] Z. Ahmed *et al.* (CDMS Collaboration), Phys. Rev. Lett. **102**, 011301 (2009).
[37] D. S. Akerib *et al.* (CDMS Collaboration), Phys. Rev. D **72**, 052009 (2005).
[38] Throughout this work the unit keV shall refer to true recoil energy whereas $\mathrm{keV_{ee}}$ are units of electron-equivalent recoil energy. This means that an ionization yield $y = E_q/E_r = 1$ is assumed when the energy is calculated from the measured signal.
[39] R. Agnese *et al.* (CDMS Collaboration), Phys. Rev. Lett. **111**, 251301 (2013).
[40] C. E. Aalseth *et al.* (CoGeNT Collaboration), Phys. Rev. D **88**, 012002 (2013).
[41] G. Angloher *et al.*, Eur. Phys. J. C **72**, 1971 (2012).
[42] C. E. Aalseth *et al.* (CoGeNT Collaboration), Phys. Rev. Lett. **106**, 131301 (2011).
[43] R. Bernabei *et al.*, Eur. Phys. J. C **67**, 39 (2010).
[44] J. Hellmig *et al.*, Nucl. Instrum. Methods Phys. Res., Sect. A **444**, 308 (2000).
[45] D. Akerib *et al.*, Nucl. Instrum. Methods Phys. Res., Sect. A **591**, 476 (2008).
[46] B. Neganov and V. Trofimov, Otkryt. Izobret. **146**, 215 (1985).
[47] P. N. Luke, J. Appl. Phys. **64**, 6858 (1988).
[48] R. C. Alig and S. Bloom, Phys. Rev. Lett. **35**, 1522 (1975).
[49] J. Lewin and P. Smith, Astropart. Phys. **6**, 87 (1996).
[50] S. Butterworth, Exper. Wireless and the Wireless Eng. **7**, 536 (1930).
[51] W. Press, B. Flannery, S. Teukolsky, and W. Vetterling, *Numerical Recipes in C: The Art of Scientific Computing* (Cambridge University Press, Cambridge, England, 1992).
[52] S. Golwala, Ph.D. thesis, University of California, Berkeley, 2000.
[53] V. Mandic *et al.*, in AIP Conf. Proc. **605**, 509 (2002).
[54] Z. Ahmed, Ph.D. thesis, California Institute of Technology, 2012.
[55] A. G. Abramov, N. A. Galyaev, V. I. Garkusha, J. Hylen, F. N. Novoskoltsev, A. D. Ryabov, and V. G. Zarucheisky, Nucl. Instrum. Methods Phys. Res., Sect. A **485**, 209 (2002).
[56] We reject events that have phonon pulse multiplicities at least 4 larger than the charge pulse multiplicity. Further, if the phonon pulse multiplicity is 3 we reject events with charge multiplicity 0.
[57] J. Lindhard *et al.*, Mat. Fys. Medd. K. Dan. Vidensk. Selsk **33**, 10 (1963).
[58] Specifically the form $\sigma_y(E_r \leq \bar{E}) = c \cdot E_r^d$ and $\sigma_y(E_r > \bar{E}) = e$ was used, where c, d, e, and $\bar{E}$ (the energy threshold) are fitted parameters.
[59] D. S. Akerib *et al.* (CDMS Collaboration), Phys. Rev. Lett. **96**, 011302 (2006).
[60] J. Zhang, Ph.D. thesis, University of Minnesota, 2014.
[61] Note the ERs and NRs have less clear "surface discrimination" within the respective populations. The difference between ERs and NRs arises because Luke phonons produce a fast-rising component due to their ballistic nature and consistent near-surface production component. ERs give a greater fraction of Luke phonons, so will generically be faster.
[62] T. J. Hofer, Ph.D. thesis, University of Minnesota, 2014.
[63] K. Pearson, Philos. Mag. Ser. 6 **2**, 559 (1901).
[64] I. T. Nabney, *NETLAB: Algorithms for pattern recognitions* (Springer, New York, 2002).
[65] J. M. Kiveni, Ph.D. thesis, Syracuse University, 2012.
[66] J. Filippini, Ph.D. thesis, University of California, Berkeley, 2008.
[67] J. Sander, Ph.D. thesis, University of California, Santa Barbara, 2007.
[68] J. R. Klein and A. Roodman, Annu. Rev. Nucl. Part. Sci. **55**, 141 (2005).
[69] G. Cowan *et al.* (Particle Data Group), Phys. Rev. D **86**, 010001 (2012), see Sec. Statistics, p. 390.
[70] I. Ruchlin and R. W. Schnee, Nucl. Instrum. Methods Phys. Res., Sect. A **664**, 336 (2012).
[71] R. Agnese *et al.* (SuperCDMS Collaboration) (to be published).
[72] V. Kudryavtsev, Comput. Phys. Commun. **180**, 339 (2009).
[73] S. Kasahara, Ph.D. thesis, University of Minnesota, 1997.
[74] W. B. Wilson *et al.*, in *Proceedings of the 12th Biennial Topical Meeting of the American Nuclear Society/Radiation Protection and Shielding Division, Santa Fe, NM, April 14–18, 2002* (American Nuclear Society, La Grange Park, IL, 2002).
[75] W. Wilson *et al.*, Radiation Protection Dosimetry **115**, 117 (2005).
[76] W. Charlton *et al.*, Nucl. Instrum. Methods Phys. Res., Sect. A **140**, 1 (1998).
[77] S. Yellin, Phys. Rev. D **66**, 032005 (2002).
[78] M. C. Smith *et al.*, Mon. Not. R. Astron. Soc. **379**, 755 (2007).
[79] J. Lavalle and S. Magni, Phys. Rev. D **91**, 023510 (2015).
[80] R. Bernabei *et al.*, Phys. Lett. B **389**, 757 (1996).
[81] P. Agnes *et al.*, Phys. Lett. B **743**, 456 (2015).
[82] E. Aprile *et al.*, Phys. Rev. Lett. **109**, 181301 (2012).
[83] D. Akerib *et al.* (LUX Collaboration), Phys. Rev. Lett. **112**, 091303 (2014).
[84] R. Agnese *et al.* (SuperCDMS Collaboration), Phys. Rev. Lett. **112**, 241302 (2014).
[85] G. Angloher *et al.*, Eur. Phys. J. C **74**, 3184 (2014).
[86] C. Savage, G. Gelmini, P. Gondolo, and K. Freese, J. Cosmol. Astropart. Phys. 04 (2009) 010.
[87] N. Anand, A. L. Fitzpatrick, and W. C. Haxton, Phys. Rev. C **89**, 065501 (2014).
[88] K. Schneck *et al.* (SuperCDMS Collaboration), Phys. Rev. D **91**, 092004 (2015).